

Highlights

- Anoxic water-rock experiments conducted as a function of $p\text{CO}_2$ at 25 °C
- Fe(II)-carbonate nucleation only reached in isolation from atmospheric CO_2
- Subsurface carbonate formation dominated carbon burial in the early Martian crust

Unravelling surface and subsurface carbon sinks within the early Martian crust

Lucy E. Kissick^{a,b,*}, Tamsin A. Mather^a, and Nicholas J. Tosca^{a,c}

^a *Department of Earth Sciences, University of Oxford, Oxford, UK*

^b *Present address: National Nuclear Laboratory, Cumbria, UK*

^c *Present address: Department of Earth Sciences, University of Cambridge, Cambridge, UK.*

**lucy.kissick@uknln.com*

ABSTRACT

Understanding the climate history of Mars, one of our closest planetary neighbours, has important implications for understanding the environmental evolution of Earth and other rocky planets in general. The widespread recognition of an extensive sedimentary record modified, at least in part, by liquid water, holds much promise to provide evidence about Mars' past. However, unravelling the pressure and compositional history of Mars' Noachian atmosphere has remained problematic. Based on expected outgassing behaviour, observed atmospheric isotope ratios, and climate models, carbon dioxide is widely considered a main constituent of the early Martian atmosphere. If this was indeed the case, it is surprising that carbonate minerals, the expected sinks for this carbon, are only abundant in a few isolated localities across the Martian surface. Three broad possibilities may account for this apparent inconsistency: (1) carbonates formed under $p\text{CO}_2$ higher than present but were buried, or subsequently destroyed; (2) Noachian atmospheric $p\text{CO}_2$ was significantly lower than current estimates; or (3) low-temperature carbonate formation was kinetically controlled under the aqueous conditions that

characterised much of the early Martian surface. While orbital spectroscopic investigations have yielded an increasing inventory of isolated carbonate-bearing deposits, their relative rarity at the near-surface has prompted suggestions that the Noachian atmosphere was commonly characterised by low $p\text{CO}_2$. Without a more complete investigation of the carbonate-forming processes occurring within the ancient crust, no hypothesis can be tested robustly. Here, we examine the controls on Fe(II)-carbonate precipitation in low-temperature, anoxic water-rock systems as a function of $p\text{CO}_2$. In experiments lasting up to 85 days, no measurable Fe(II)-carbonate precipitation occurred within the limits of analytical detection, despite significant and sustained supersaturation with respect to siderite. These observations are quantitatively consistent with recent investigations highlighting a significant supersaturation threshold for Fe(II)-carbonate nucleation. Reaction path models that incorporate these constraints indicate that Fe(II)-carbonate supersaturation thresholds would have been commonly met in low water:rock ratio systems isolated from the Noachian atmosphere as opposed to high water:rock ratio, open-systems exposed at the near surface. These results suggest the rarity of carbonates exposed at or near the surface of Mars may be controlled, at least in part, by a lack of deep crustal exposures and lack of the geochemical conditions conducive to carbonate formation, rather than insufficient atmospheric $p\text{CO}_2$. Such geochemical constraints are in turn consistent with available orbital geological data indicating that carbonates may be more abundant within the deep crust, potentially representing a significant subsurface carbon sink.

KEYWORDS

Noachian Mars, siderite, carbonate, Martian atmosphere, experimental geochemistry.

1. INTRODUCTION

The early evolution of rocky planetary bodies is archived by the minerals deposited within their crusts. Plate tectonics has obliterated the geological record of the first ~1 billion years of Earth's history. Mars has not experienced crustal destruction in the same manner as Earth, and the recent discovery of an extensive and ancient sedimentary record on Mars offers a unique opportunity to understand Earth's earliest evolution in the context of other rocky planetary bodies (Malin and Edgett, 2000; McLennan et al., 2019). Yet, although the last two decades of Mars exploration have shown that liquid water shaped much of the planet's ancient sedimentary record, the early evolution of the Martian climate has endured as a major problem in modern planetary science. It is generally assumed that CO₂ has always remained the dominant constituent of the Martian atmosphere, as observed today (Owen et al., 1977; Wordsworth et al., 2017), but climate models have shown that a thick CO₂ atmosphere alone could not have produced a greenhouse effect sufficient to stabilise liquid water in the context of a faint young sun (Sagan and Chyba, 1997). Accordingly, a lack of constraints on both the total atmospheric pressure as well as the identity of both major and minor atmospheric constituents have fuelled active debate as to how liquid water was stabilised over geologically significant timescales (Pollack et al., 1987; Wordsworth et al., 2017).

More information about the Martian sedimentary record also leads to further unknowns in terms of how to interpret it in relation to past atmospheric composition. As geochemical considerations indicate that liquid water and a CO₂-rich atmosphere should produce carbonate minerals, their apparent scarcity on both the ancient and extant Martian surface has persisted as a conundrum (Fairén et al., 2004; Ehlmann et al., 2008; Michalski et al., 2013). Carbonate minerals have long been recognised as minor pre-terrestrial alteration phases within Martian

meteorites (see Bridges et al., 2019, for summary), and as minor or trace components of surficial dust (Bandfield et al., 2003) and soils (Boynton et al., 2009) but they are rarely exposed in significant quantities at the surface. Numerous hypotheses have sought to explain this rarity, including formation and subsequent burial or destruction (Ehlmann et al., 2008; Michalski and Niles, 2010), kinetic competition with clay minerals (Michalski et al., 2015), insufficient $p\text{CO}_2$ (Bristow et al., 2017), loss of CO_2 to space (Jakosky, 2019), or suppression by widespread acidic fluids (Fairén et al., 2004), but these hypotheses have proven difficult to test against the geological record. Alternatively, oxalates have been recently suggested as a possible terminal C-sink within the Martian crust (Franz et al., 2020), but the global importance of this potential sink is unknown at present.

The problem of carbonate formation on ancient Mars was further intensified when NASA's Mars Science Laboratory (MSL) mission obtained evidence for a redox-stratified lacustrine environment preserved within the sedimentary rocks at Gale Crater (Hurowitz et al., 2017). This depositional system commonly featured Fe^{2+} and geochemical/mineralogical characteristics consistent with circum-neutral pH — favourable conditions for carbonate production in the presence of a CO_2 -rich atmosphere (Pollack et al., 1987). Yet, carbonate minerals remain well below 1 wt. % within these rocks, although reach a maximum of ~1-2 wt. % in some aeolian materials (Ming et al., 2014; Franz et al., 2020). On the basis of kinetic and thermodynamic relationships, these results were taken to reflect an ancient atmosphere featuring low $p\text{CO}_2$ — a problematic result for all current models of atmospheric and climatic evolution (Bristow et al., 2017). However, experimental and theoretical data raised the possibility that Fe(II)-carbonate production within Gale Crater sedimentary rocks was instead

subject to strong kinetic controls, which may have in turn influenced the distribution of carbonates within the ancient crust (Tosca et al., 2018).

In apparent contrast with data obtained from sedimentary rocks, some investigations have identified regionally significant accumulations of carbonate within exhumed deep-crustal rocks (Michalski and Niles, 2010; Wray et al., 2016), and isolated surface or near-surface deposits (Ehlmann et al., 2008; Morris et al., 2010; Edwards and Ehlmann, 2015). Together, these observations indicate that while carbonate formation was favoured in some geochemical systems, the mechanisms controlling carbonate formation, and therefore the cycling of carbon between the early Martian crust and atmosphere, are poorly constrained (Tosca et al., 2018; Franz et al., 2020). This precludes attempts to reconstruct palaeo-climatic conditions from the geological record, a particularly urgent problem given that NASA's *Perseverance* rover will soon investigate carbonate-rich sedimentary strata hosted at Jezero Crater (e.g., Ehlmann et al., 2008; Horgan et al., 2020).

Upon aqueous alteration under mildly acidic conditions at relatively low temperature (<50 °C), cations should be released in proportions controlled by a largely basaltic Martian crust (Milliken et al., 2009). Thus, under a CO₂-bearing atmosphere, Fe- and Mg-carbonates, and to a lesser extent Ca-carbonates, should be produced. Mg-rich carbonates are kinetically controlled such that their precipitation at low temperature is typically confined to highly alkaline environments that initially generate metastable hydrous phases such as hydromagnesite and nesquehonite, rather than its geologically stable form, magnesite (Königsberger et al., 1999; Power et al., 2019). CaCO₃, on the other hand, readily forms in some arid basaltic soils on Earth, although these environments reflect largely oxic conditions with cation budgets that can be influenced by sea-spray aerosols (Whipkey et al., 2000, 2002). How this picture might change in

completely anoxic systems, however, is more difficult to evaluate. For example, experiments and numerical modelling of low-temperature basalt-water interactions under Earth's currently oxic atmosphere show that the kinetics of Fe(II)-oxidation outpace Fe(II)-carbonate precipitation as pH (and therefore carbonate saturation states) increases (i.e., Gysi and Stefansson, 2012). Thus, although Ca- and Mg-carbonate formation cannot be discounted, by molar proportion, Fe(II)-carbonate precipitation should represent a quantitatively important carbon sink within the Martian crust, especially given that, on average, Martian basalts feature FeO concentrations two times higher than most terrestrial basalts (Wade et al., 2017). Consistent with this expectation, pre-terrestrial carbonates in Martian meteorites are overwhelmingly dominated by Fe(II), and siderite appears more common than previously thought in outcrops that sample deeper portions of the ancient Martian crust (Wray et al., 2016; Bridges et al., 2019). Nevertheless, there is little empirical data to predict the extent of Fe(II)-carbonate formation under anoxic conditions at low temperatures — a key component in developing a more complete understanding of carbonate deposition within the Martian crust.

To address these problems, we experimentally investigate anoxic water-rock interactions to examine the processes that control the precipitation of Fe(II)-carbonate minerals from a largely basaltic surface at 25 °C. We place these results in a broader geochemical context by examining kinetic controls on Fe(II)-carbonate formation, identified from our experiments, with reaction path models of water-rock interaction. We then contextualise our observations within the current inventory of surface carbonates on Mars to understand the factors controlling their formation and distribution.

2. MATERIALS AND METHODS

2.1. Experiments

The focus of our experimental approach is to examine and constrain the parameters that promote Fe(II)-carbonate formation from the dissolution of rock-forming ferromagnesian minerals. To isolate the Fe(II)-carbonate system and simplify the experimental approach, we first examined interactions between water and Fe-bearing olivine (fayalite: Fe_2SiO_4 , Fo_0), which is the most reactive of rock-forming silicates found within the Martian crust (Velbel, 1999). As aqueous Fe chemistry may be influenced by the catalytic activity of minerals that commonly occur with natural fayalite, we chose to synthesise pure fayalite to be sure what reactions we were studying. Although the chemical composition of olivine in many igneous and sedimentary rocks on Mars is known to contain appreciable Mg (Vaniman et al., 2014), our experiments featured pure synthetic fayalite or physical mixtures of synthetic fayalite and natural forsterite. Large, optically pure individual crystals of forsterite were hand-picked from a natural specimen, crushed, then sieved to the desired particle size (average $0.0554 \text{ m}^2/\text{g}$). Mineralogical purity was confirmed via powder X-ray diffraction.

To synthesise 10 g fayalite, 2.9485 g of SiO_2 and 7.8365 g of Fe_2O_3 , (Alfa Aesar; 99.5 % purity), were heated to 800°C to remove volatiles. The materials were thoroughly homogenised in an agate pestle and mortar, pelletised under 4 metric tonnes of pressure into 2-3 g individual pellets, placed in an alumina crucible, and heated in a furnace for 3 hours. Temperatures were 1080°C : as high as possible to accelerate reaction kinetics, but below the fayalite melting point of $\sim 1200^\circ\text{C}$. To prevent the formation of more oxidised Fe-phases such as wüstite or magnetite, we fixed oxygen fugacity (f_{O_2}) at this temperature between the iron-wüstite and wüstite-magnetite buffers ($\log f_{\text{O}_2} = -12.5$) by utilising a gas flow mixture of 84 mL/s CO and 114 mL/s CO_2 to reduce Fe(III). When analysed via BET (Brunauer-Emmett-Teller) surface area analysis

using the Micromeritics 3flex facilities at the Chemistry Research Laboratory, University of Oxford, the average specific surface area for fayalite was $0.3 \text{ m}^2/\text{g}$, with an estimated precision of ~ 10 relative percent.

All water-rock interaction experiments were conducted within a Coy polymer anoxic glovebox with an atmosphere of 4 % H_2 /96 % N_2 . Trace O_2 was scrubbed from the system by a Pd catalyst, which produces H_2O as a by-product, which is then removed via adsorption onto an anhydrous CaSO_4 desiccant. The gas composition of the anoxic chamber was continuously monitored with a Coy gas analyser and the atmosphere maintained at $<1 \text{ ppm O}_{2(\text{g})}$ for the duration of all experiments, sample preparation, and analysis. All experiments were conducted at $25 \text{ }^\circ\text{C}$ ($\pm 1.5 \text{ }^\circ\text{C}$) within 0.172 L Nalgene serum bottles sealed with 1 cm butyl-rubber caps, wrapped in Al-foil to prevent photo-oxidation (Braterman et al., 1984), and continuously stirred on an orbital shaker. pH and oxidation-reduction potential (ORP) were data-logged using Ag/AgCl combination pH and platinum ORP electrodes. The pH electrode was calibrated with NIST standard buffer solutions (pH 4 and 7) and the ORP electrode with ZoBell's solution (Nordstrom, 1977). Based on the periodic measurement of calibrant standards, precision for pH was ± 0.05 (1σ).

All aqueous solutions were made with deionised Milli-Q first purged of dissolved O_2 by bubbling O_2 -free N_2 gas through the solution for at least 45 minutes (Butler et al., 1994) before transfer to the glovebox. The water was then stirred for 1 hour in the anoxic atmosphere and left for at least 24 hours to allow any residual O_2 to escape. We used dilute sulphuric acid (H_2SO_4) to fix the starting pH of each experiment to either 2 or 4. This is because Martian meteoric water may have commonly featured low pH due to the input of volcanic volatiles such as H_2SO_4 or HCl (Hurowitz et al., 2010). This may have been continuously provided to Martian soils as

183 meteoric water, enabling through-flow systems and transport phenomena relevant under specific
184 circumstances.

185 Total dissolved inorganic carbon (DIC) concentrations for each experiment were chosen
186 to equate to saturation with either a 0.1, 0.5, or 1.0 bar CO₂ atmosphere under the desired initial
187 pH. DIC was initially set with freshly prepared sodium bicarbonate (NaHCO₃) stock solutions.

188 To minimise degassing of CO₂ over the course of experiments, headspace in reaction
189 vessels was eliminated by completely filling each vessel with solution and sealing with gas-tight
190 septum caps. Solution samples (each 1 % of solution volume) were withdrawn via 0.1 µm
191 syringes through the septum caps. The samples were then syringe-filtered to 0.22 µm. In total, 10
192 solution samples were collected from each experiment, except from low water-rock ratio
193 experiments, where solution volume did not allow repeated sampling; in these cases, one sample
194 was extracted at experiment termination. Experiments lasted between 12 hours and 85 days. 86
195 individual experiments form the basis of the discussion in this paper.

196 Four groups of experiments were conducted, detailed in Table 1. These experiments vary
197 in dissolved CO₂ concentration, water-rock ratio, and initial pH of the solution to examine a
198 variety of conditions conducive to the saturation and precipitation of Fe(II)-carbonate.

199 Elemental analysis of solution samples was performed via inductively coupled optical
200 emission spectrometry (ICP-OES) at the Scottish University Environmental Research Centre,
201 University of Glasgow, and also via mass spectrometry (ICP-MS) in-house at the Department of
202 Earth Sciences, University of Oxford. 0.15 mL samples of solution were acidified with 14.75 mL
203 of O₂-free 5 % HNO₃ to prevent the formation of solid phases before analysis.

204 Upon experiment termination, solutions were vacuum-filtered through a 0.22 µm nylon
205 membrane and solids left to dry within the glovebox. Solids were analysed in-house via powder

X-ray diffraction (XRD) using a PANalytical Empyrean Series 2 X-ray diffractometer with a Co $K\alpha_1$ source operated at 40 kV and at 40 mA, scanned between 5 and 80 degrees 2θ . Powders were loaded onto single crystal silicon sample holders and wrapped with Kapton film within the glovebox to minimise oxidation during analysis.

Scanning electron microscopy (SEM) was performed using a FEI Quanta 650 FEG on selected, uncoated samples to characterise the morphology of solid materials and identify any minor phases below XRD detection levels (estimated at 1-5 wt. % depending on the nature of the crystalline phase). A small amount of solid was mounted on a carbon stub within the glovebox, then transferred into the evacuated SEM chamber. Energy dispersive X-ray spectrometry (EDS) was also performed using this SEM for *in situ*, semi-quantitative, compositional analysis.

To additionally identify and characterise the presence of secondary minerals, transmission Fourier transform infrared spectroscopy (FT-IR) was performed using a PerkinElmer Frontier mid-IR spectrometer on powdered solid samples mixed with KBr powder at a KBr-sample ratio of ~1:200. These samples were ground together, pelletised at 7 metric tonnes, and analysed within 20 minutes of exposure to air. Measurements were collected from between 400 to 4000 cm^{-1} at 1 cm^{-1} resolution. We estimate the minimum detection limits for carbonate phases within our samples at ~0.8 wt. % following standardisation procedures outlined in Vagenas et al. (2003).

2.2. Geochemical modelling

To more broadly investigate a range of environmental parameters on the evolution of solution chemistry during water-rock interaction, we adapted the kinetic model used in Tosca et al. (2018) in the software *The Geochemist's Workbench* (version 12, Bethke, 2017), which uses

thermodynamic data from the Lawrence Livermore National Laboratory (LLNL) database (Delany and Lundeen, 1991). The model computes mineral dissolution rates according to the following equation:

$$r = A_S k_+ a_{H^+}^n \left(1 - \frac{Q}{K}\right) \quad (\text{eq. 1})$$

where r is the rate of dissolution, A_S is the surface area (cm^2), k_+ is the rate constant ($2.34 \times 10^{-11} \text{ mol cm}^{-2} \text{ sec}^{-1}$ for both fayalite and forsterite; Bandstra and Brantley, 2008), a_{H^+} is the dissolution reaction's dependence upon the concentration of protons to the power of n (where n was determined to be 0.372 by Bandstra and Brantley, 2008), Q is the activity product and K the equilibrium constant for the dissolution reaction.

The reaction path model introduces free quantities of fayalite and/or forsterite to a dilute 1 kg solution and iteratively solves the equilibrium state of the system as a function of the reaction progress variable. pH was allowed to evolve until steady state conditions were reached. Four key parameters were varied in each model: (1) water:rock ratio (1:1 or 1:500, approximating subsurface/surface waters respectively); (2) particulate specific surface area with values (100 or 1000 cm^2/g) reflecting varying estimates for San Carlos olivine ($\sim 40\text{-}840 \text{ cm}^2/\text{g}$ from the study of Brantley and Mellott, 2000, and our own BET analyses, which together represent realistic estimates of minimum and maximum olivine particle surface areas typical of this mineral, and thus the surface available for reaction); (3) dissolved CO_2 content (equating to 0.1 or 1.0 bar CO_2); and (4) open versus closed system conditions with respect to CO_2 (simulating a water in constant contact with the atmosphere, or a subsurface aqueous system isolated from the atmosphere, respectively).

3. RESULTS

3.1. Temporal evolution of solution chemistry

The temporal evolution of solution chemistry during water-rock interaction is controlled by mineral dissolution and, once secondary mineral phases become supersaturated, mineral precipitation. The fayalite dissolution rate, as for many other rock-forming silicate minerals, is controlled by a number of factors, but principally pH, particle surface area, temperature, and the degree of undersaturation (which is typically a function of the Gibbs free energy change of the dissolution reaction; (Aagaard and Helgeson, 1982; Lasaga, 1998). As H^+ is consumed and cations are released to solution during the dissolution reaction, pH increases, which decreases dissolution rate accordingly. As a consequence, closed-system water-rock experiments typically exhibit an initial rapid phase of chemical change, followed by a gradual change to steady state (e.g., Qafoku et al., 2012). This relationship is directly observed in **Figure 1**, which illustrates the pH pathway (a), dissolved Fe (b), dissolved SiO_2 (c), and Fe/Si ratio (d) over time for a typical fayalite-bearing experiment. As this particular experiment was run for over two months, the time intervals between each extraction do not permit visualisation of the rapid initial dissolution kinetics that were observed for other experiments sampled more frequently across the first days (for the full set of experimental data, see **Supplementary Data**). The Fe/Si ratio in **Figure 1d** indicates that dissolution is, in some cases, non-stoichiometric with respect to Fe and Si, with Fe/Si ratio reaching 1.7-2.2. **Figure 1d** shows the preferential release of Fe in solutions begun at an acidic pH, while for experiments begun at pH 4 this is slightly closer to stoichiometric. The precipitation of Si from solution as amorphous Si (discussed below) is likely

to have removed Si from solution, increasing the Fe/Si ratio over the course of these experiments.

3.2. Siderite saturation

To assess the evolution of our experiments with respect to siderite saturation state, **Figure 2** shows all solution data as a function of Fe^{2+} activity and pH at three different DIC concentrations (which are proportional to the three $p\text{CO}_2$ conditions explored at fixed initial pH of 2 or 4; **Table 1**). Fe^{2+} activities were obtained from solution concentrations by iteratively calculating the ion activity coefficients and ionic strength for all dissolved aqueous species using the B-dot equation (Helgeson and Kirkham, 1974), and dissociation constants for carbonic acid (K_1 and K_2 ; (He and Morse, 1993). Here saturation state with respect to siderite is defined as:

$$\Omega(\text{siderite}) = \frac{a_{\text{Fe}^{2+}} \times a_{\text{CO}_3^{2-}}}{K_{sp}} \quad (\text{eq. 2})$$

where Ω is the ratio between K_{sp} and the Ion Activity Product (IAP, which equals the activities of Fe^{2+} and CO_3^{2-} multiplied together), K_{sp} is the solubility product for siderite ($10^{-10.24}$; Singer and Stumm, 1970), and $a_{\text{CO}_3^{2-}}$ is the activity of CO_3^{2-} . For reference, the equilibrium solubility line for siderite is plotted on **Figure 2**. We have opted to use this simple approach, rather than adopt a speciation model for aqueous Fe(II) chemistry, because speciation models are poorly constrained and not supported by available data (**Jiang and Tosca, 2020**). An important assumption behind this figure is that solution DIC is fixed (i.e., there is no significant exchange between headspace and solution) and that carbonate mineral precipitation is effectively none over the course of the experiment, thus leaving the solution DIC pool largely unaltered. As pH

and dissolved Fe^{2+} concentration (and therefore Fe^{2+} activity) generally increase throughout the course of an experiment, experimental solutions progressively evolve toward higher supersaturation with respect to siderite (**Figure 2**). Experiments begun at pH 2 (in red) consistently display the highest Fe^{2+} activities, reflecting greater amounts of fayalite dissolution in acidic solutions, but experiments begun at pH 4 (in blue) consistently reach the highest pH levels owing to their higher initial pH and thus lower buffer capacity against alkalinity generated by silicate dissolution.

The three graphs in **Figure 2** suggest that all experiments evolve to varying levels of supersaturation with respect to siderite, and that some experiments evolve to exceedingly high supersaturation levels. As expected from equilibrium carbonate chemistry, siderite saturation state is maximised with high pH and, to a lesser extent, high Fe^{2+} activity, for a given fixed DIC pool.

3.3. Fe(II)-silicate and amorphous SiO_2 formation

An additional factor that may influence the nucleation and subsequent precipitation of siderite is the precipitation of other Fe-bearing phases. In the fayalite-water system investigated here, Fe(II)-silicate precipitation constitutes one such process. The Fe(II)-silicate greenalite ($\text{Fe}^{\text{II}}_3\text{Si}_2\text{O}_5\text{OH}_4$), like siderite, precipitates under anoxic conditions at circum-neutral pH (Tosca et al., 2016) and this kinetic competition may have influenced biogeochemical cycles on the Archaean Earth (Jiang and Tosca, 2019).

Figure 3, a solubility diagram for the Fe^{2+} - SiO_2 - H_2O system, encompasses the dominant controls on greenalite, which are pH, the activity of SiO_2 , and the activity of Fe^{2+} . In **Figure 3**, the apparent solubility of greenalite, as estimated by Tosca et al. (2016) ($\log K_{\text{sp}} = 27.6$),

provides a reference for chemical conditions likely to trigger Fe(II)-silicate nucleation, with the supersaturation of amorphous Si estimated by the exceeding of the dashed line (Siever, 1992). In **Figure 3**, datapoints from experiments begun at both pH 2 and 4 (red and blue) exceed the apparent solubility of greenalite across all DIC concentrations. The figure also indicates that all experiments conducted under lower initial pH are supersaturated with respect to amorphous silica. Amorphous silica precipitation in these experiments is consistent with the earlier observation of non-stoichiometric Fe/Si release (**Figure 1**). From these constraints on the stoichiometry of dissolution, we can quantify the amount of amorphous silica by assuming that the $\text{SiO}_{2(\text{aq})}$ not released into solution (therefore resulting in non-stoichiometric solution Fe/Si levels) has all precipitated as amorphous silica. From this, we estimate that a total of 6×10^{-4} moles of amorphous silica precipitated over the course of the experiment.

3.4. Solid phase characterisation

XRD, FT-IR, and SEM were all employed to examine whether secondary minerals precipitated over the course of the experiments. XRD analysis did not identify any new mineral phases: no new diffraction peaks were observed relative to unaltered fayalite or forsterite-fayalite mixtures (**Supplementary Figure 1**). This indicates that no additional crystalline phases are present above the detection limits of the instrument, which, under the analysis conditions used here, corresponds to approximately 5 wt %.

FT-IR analysis offers a more sensitive evaluation of both crystalline and non-crystalline phases present. FT-IR transmission spectra show no indication of the presence of carbonates. For example, the most intense absorption for carbonates arises from CO_3^{2-} stretching within the

mineral lattice (Farmer, 1974); this is located at $\sim 1350\text{-}1500\text{ cm}^{-1}$ for rhombohedral carbonate minerals, but is absent from all spectra (**Supplementary Figure 2**).

In addition to XRD and FT-IR, SEM was employed to examine morphological changes between reacted and unreacted solids. This analysis revealed no clear evidence of secondary Fe-carbonate phases, including characteristic morphologies observed in other synthetic studies (e.g., (Jimenez-Lopez and Romanek, 2004; Qafoku et al., 2012; Jiang and Tosca, 2019). However, in several experiments conducted for 85 days (the longest period run), with both fayalite and forsterite present, evidence for secondary mineral formation was observed upon the fayalite grains under all CO_2 levels and begun at both pH 2 and 4. The secondary precipitates displayed a morphology that replicated grain boundaries and interstices (**Figure 4a, b**). Given the relatively fine scale at which the precipitates occur, EDS spectra do not allow unambiguous chemical differentiation from the underlying olivine substrate, but a clear lack of euhedral morphology is consistent with the presence of amorphous silica, consistent with solution chemistry analyses discussed above.

SEM evidence also indicates a distinct secondary phase in addition to tentative amorphous silica. This phase occurred in four of the same experiments where amorphous silica was identified, and one where no silica was identified. This phase occurs as aligned, uniformly dispersed, nanometre-scale plates (**Figure 4c and d**) and was identified only either upon fayalite grains **Figure 4c** or possibly either as coalesced nuclei sometimes as large as $10\text{ }\mu\text{m}$ across or upon an aggregate material **Figure 4d**. When analysed via EDS without carbon/gold coating and at low vacuum, Fe, Si, O, and C are present; however, contribution from the fayalite and surrounding carbon adhesive cannot be discounted. While C was also identified via EDS on non-precipitate-bearing fayalite grains, as well as unreacted fayalite, this was consistently $\sim 4\text{ wt } \%$

lower than the precipitate-bearing grains, and likely reflects contribution from the surrounding carbon adhesive upon which the samples were set. If this C-bearing phase is a Fe(II)-carbonate, its negligible overall abundance and/or a potentially non/poorly-crystalline nature may render it undetectable by FT-IR and XRD.

4. DISCUSSION

4.1. Siderite precipitation kinetics

Solution-phase analyses indicate that the anoxic water-rock systems investigated here commonly feature excessive supersaturation with respect to siderite (i.e., Ω_{siderite} up to 3,610). However, despite such high supersaturation, XRD, FT-IR and SEM all indicate that the formation of secondary Fe(II)-carbonate is negligible. Taken together, these data indicate that the precipitation of Fe(II)-carbonate at 25 °C is strongly controlled by kinetics.

Mineral precipitation must be preceded first by nucleation, where constituent ions form a nucleus or cluster that is sufficiently large to be thermodynamically stable (Volmer and Weber, 1926; Lasaga, 1998). Nucleation thus occurs when this stability threshold is exceeded, which in turn corresponds to a critical threshold in solution supersaturation state. Once stable nuclei are produced and the solution remains supersaturated, crystal growth may occur. In many low-temperature aqueous systems, the homogeneous (or spontaneous) nucleation of secondary minerals from solution requires significant levels of supersaturation (Turnbull and Fisher, 1949). This varies depending on the solid phase, and is sensitive to factors such as mineral chemistry and structure, and, most importantly, mineral-solution interfacial energy (Lasaga, 1998).

For Fe(II)-carbonate, it has been long known that the effective critical supersaturation threshold at 25 °C is far higher than for other carbonates such as calcite (e.g., Jimenez-Lopez and

Romanek, 2004). Two recent experimental datasets clarify where the effective saturation threshold might lie for the homogenous nucleation of Fe(II)-carbonate. The first is outlined in Tosca et al. (2018) where the critical threshold for Fe(II)-carbonate nucleation was estimated at Ω_{siderite} values of ~ 400 . This Ω_{siderite} was exceeded in many of our experiments (**Figure 2**), including three with nano-particle precipitation observed via SEM. Jiang and Tosca (2019) also constrained the critical supersaturation associated with Fe(II)-carbonate nucleation. These authors hypothesised that under highly supersaturated conditions Fe(II)-carbonate nucleation proceeds via amorphous iron carbonate (AFC), a metastable precursor to siderite. In their study, Jiang and Tosca (2019) suggested that the AFC precursor is characterised by a different chemical composition than siderite, and that the apparent solubility of AFC effectively defines the maximum supersaturation of the Fe(II)-carbonate system at 25 °C. Plotting Jiang & Tosca (2019)'s AFC apparent solubility (the *AFC supersaturation line*) delineates conditions where AFC and thus Fe(II)-carbonate, may nucleate and precipitate. The AFC supersaturation line is plotted on three graphs in **Figure 2**, where each plot represents experiments conducted under three DIC concentrations that equate to either 0.1, 0.5, or 1.0 bars of dissolved CO₂ at initial pH of 2 or 4. Plotted upon each are the pH and dissolved Fe²⁺ content for each extracted sample (10 × samples per one experiment), which, in addition to DIC, comprise the three factors controlling Fe(II)-carbonate saturation state. Out of the data shown in **Figure 2**, only a relatively small number of individual datapoints exceed this line. This analysis provides a possible explanation for why Fe(II)-carbonate formation is apparently negligible in our system despite significant supersaturation: in light of available constraints on Fe(II)-carbonate nucleation, the conditions explored here only surpassed the nucleation threshold infrequently. For the experiments that did exceed the AFC line, solution-phase analyses and solid-phase characterisation indicate that

precipitation of Fe(II)-carbonate was negligible; even though some nanometre-scale precipitates were identified across the most saturated experiments, their formation did not control Fe and/or CO₂ concentrations in these experiments (**Figure 2**). This result can be understood in the context of ‘induction time,’ or the time elapsed between the moment supersaturation is reached and the moment nucleation occurs (Kashchiev et al., 1991). The induction time typically carries a strong exponential dependence on supersaturation state (Lasaga, 1998), and so these experiments may have been terminated before significant nucleation occurred. Consistent with this, Jiang and Tosca (2019) noted that even when AFC solubility is crossed, nucleation and apparent solubility control is relatively slow, occurring over a period of several days.

4.2. Unravelling surface and subsurface carbon sinks within the early Martian crust

Our experimental results indicate that Fe(II)-carbonate precipitation from supersaturated solutions is unlikely to occur unless a critical nucleation threshold is crossed, and that this only rarely occurred across a broad range of conditions explored in our experiments. From these results, we can best understand the distribution of these phases on Mars by posing the question: which environments hosting water-rock interaction were most likely to surpass the nucleation threshold for Fe(II)-carbonate precipitation? In other words, how would carbon burial have been distributed within the Martian crust?

To explore this in a more quantitative manner, we used reaction path models of water:rock interaction to examine how water-rock ratio, particulate surface area, dissolved CO₂ levels, and open versus closed systems with respect to CO₂ influence solution chemistry and Fe(II)-carbonate saturation states (**Figure 5**). Specifically, we examined which conditions promote Fe(II)-carbonate supersaturation levels that exceed AFC solubility estimates derived

from Jiang and Tosca (2019). These results are consistent with the general expectation that changes in alkalinity and/or DIC concentration will fundamentally control carbonate mineral saturation state (Zeebe and Wolf-Gladrow, 2001). Among the most important processes that influence alkalinity during water:rock interaction are the water:rock ratio and initial pH. Both of these parameters control how rapidly silicate mineral dissolution provides alkalinity to the solution (the rate of which is maximised by low water:rock ratios and relatively high initial pH; **Figure 5c** and **d**). However, $p\text{CO}_2$ is the most significant parameter controlling Fe-carbonate saturation, in that it controls how DIC concentrations evolve during water-rock interaction (left-hand column: 0.1 bar CO_2 ; right-hand column: 1.0 bar CO_2).

If $p\text{CO}_2$ is increased and the system remains open with respect to the atmosphere, Fe(II)-carbonate supersaturation remains relatively low, and requisite supersaturation thresholds are not crossed. These conditions would be satisfied in water:rock interaction systems which are open to the atmosphere where alkalinity contributions from silicate weathering cannot compete with acid-base CO_2 buffering from the atmosphere. Under these conditions, increased alkalinity resulting from water-rock interaction in turn results in CO_2 absorption from the atmosphere which also increases DIC concentrations. This results in reaction path trajectories in DIC-alkalinity space that evolve sub-parallel to the Fe-carbonate saturation threshold (**Figure 5a** and **b**), sustaining undersaturated conditions in atmospherically buffered systems.

Conversely, our reaction path models show that AFC solubility is commonly exceeded in systems that are closed with respect to CO_2 , such as sub-surface aquifers or ice-covered lakes (Kling et al., 2020). This is because the DIC pool is fixed, but alkalinity increases due to silicate dissolution, which drives rapid changes in Fe(II)-carbonate saturation state (i.e., vertical trajectories on **Figure 5a** and **b**). This effect has been observed in Icelandic basaltic catchments,

where the rapid consumption of CO₂ with basaltic materials drove pH to relatively high levels (Gislason et al., 1996; Perez-Fodich and Derry, 2019). This effect is further magnified at low water:rock ratio. It is worth noting here that the maximum pH levels reached in our reaction path models are limited by thermodynamic saturation with respect to olivine, which causes the dissolution rate to collapse to zero. The difference in pH between this threshold and observations in natural systems where pH may reach 9 or even 10 (i.e., Gislason et al., 1996; Perez-Fodich and Derry, 2019) may be due in part to the surface chemistry of silicate minerals and exchange reactions that consume additional protons. These reactions are thought to account for the observation that the “immersion pH” of Ca/Mg-rock forming silicates in pure or dilute water ranges from ~9-11 (Oelkers et al., 2009; Pokrovsky and Schott, 2000). These surface proton exchange reactions are not accommodated in our model. Nevertheless, by extension, our results indicate that environments most likely to favour Fe(II)-carbonate formation at low temperature involve low water:rock ratio and a closed system with respect to CO₂ (but relatively high initial *p*CO₂ or DIC concentrations). This includes, for example, subsurface environments which feature infiltration by CO₂-charged meteoric water. Carbonate formation has also been advocated within lacustrine systems (i.e., open system conditions), though constraints on the temperature of carbonate precipitation are lacking for these examples and geological evidence indicates that contribution from magmatic- or impact-hosted hydrothermal waters cannot be ruled out (e.g., Ruff et al., 2014; Brown et al., 2020; Horgan et al., 2020). *In-situ* constraints on open system lacustrine systems on early Mars show that siderite was absent from the primary mineral assemblage even though such environments were characterised by intermittent subaerial exposure and potential evaporative concentration (Ming et al., 2014; Stein et al., 2018).

Although constraints from reaction path modelling illuminate the controls on Fe(II)-carbonate supersaturation in water-rock systems on early Mars, kinetic controls on the precipitation of non-carbonate Fe-phases (i.e., Fe-oxides, Fe-silicates, etc.) undoubtedly also played an important role in the distribution of Fe-carbonates. These were not considered explicitly in the reaction path models explored here because of a general lack of robust kinetic data for these phases. In anoxic systems, pH levels at circum-neutral or higher favour the precipitation of Fe(II)-oxides and Fe(II)-silicates in addition to Fe(II)-carbonate (Ruff et al., 2014; Horgan et al., 2020; Brown et al., 2020). Although available data do not permit quantitative assessments of Fe(II)-silicate formation from a kinetic standpoint, experiments show that Fe(II)-silicate formation rates are relatively slow under supersaturated conditions, similar to Fe(II)-carbonates. However, clay formation on Mars appears to have been relatively efficient over geological timescales — over 70 % of Martian smectites, the most common clay identified, are classed as Fe-rich (Michalski et al., 2015). Similarly, clays and carbonates are rarely found contemporaneously on Mars (Ehlmann et al., 2012), and where they are, they are Mg-rich (e.g., Ehlmann et al., 2008). This may indicate that clay formation proceeded under conditions not typically conducive to Fe(II)-carbonate formation, that Fe-bearing clays efficiently outcompeted carbonate phases for Fe, or that Fe-carbonates were poorly preserved over geological timescales relative to clay minerals.

In addition, magnetite, as on the early Earth, competed with siderite for Fe on early Mars. Tosca et al. (2018) presented experimental data showing that, under some conditions, Fe(II)-oxide formation (and subsequent transformation to green rust and magnetite) outpaces Fe(II)-carbonate nucleation. None of our experiments reached $\text{Fe}(\text{OH})_2$ saturation, which would be surpassed by exceeding a $\log(a_{\text{Fe}^{2+}}/a_{\text{H}^+}^2)$ value of 14.0 (Feitknecht and Schindler, 1963) on

Figure 3. However, the reactive transport models of Tosca et al. (2018) showed these conditions were maximised at the interface between lake bottom water and groundwater in the Gale Crater lacustrine system, and may not reflect water-rock interaction within the basaltic crust more generally.

Taken together, our experimental results and reaction path modelling provide kinetic insight on the known distribution of carbonates within the Martian crust. Although Mg-bearing carbonates have been recognised from *in-situ* rover data and orbital spectroscopy, data indicate that hydrothermal processes may have played an important role in their formation (e.g., Ehlmann et al., 2008; Morris et al., 2010). Fe-bearing carbonates, however, appear to be mostly focused in exhumed crustal rocks potentially sampling the deep subsurface (e.g., Michalski and Niles, 2010; Michalski et al., 2013). For instance, siderite has been identified within excavated crustal exposures from up to 6 km deep (Michalski and Niles, 2010). Such exposures from the deep subsurface are rare, but increasingly detailed surveys continue to yield evidence for further siderite-bearing outcrops (e.g., Wray et al., 2016). Siderite has also long been recognised as a component of pre-terrestrial alteration assemblages in Martian meteorites thought to have been formed predominantly by sub-surface fluids (e.g., Bridges et al., 2019). Siderite hosted in Martian meteorites suggests these samples were once part of such a favourable geochemical environment: many of them appear to record low water:rock ratio, closed system conditions most favourable to overcoming kinetic influences on Fe(II)-carbonate nucleation discussed above (e.g., Halevy et al., 2011). Together, this pattern is consistent with the experimental and theoretical constraints on Fe(II)-carbonate formation presented here.

Deep crustal exposures into the Noachian crust may also represent preservational windows into warm, Fe²⁺-rich, neutral-to-alkaline environments once in contact with CO₂-

bearing fluids; however, the geochemical characteristics of these environments are comparatively less constrained. Nevertheless, experimental and theoretical constraints provide a framework for understanding why carbonate formation should have apparently been favoured within the subsurface, and this reservoir has yet to be exhaustively characterised. New constraints are likely to emerge as the *Perseverance* rover investigates sedimentary rocks that were at least partly derived from such a carbonate-rich crustal environment (e.g., Ehlmann et al., 2008), with orbital spectroscopy suggesting a detrital/deltaic origin for the carbonates at Jezero Crater, including evidence for carbonate-cemented point bar deposits (e.g., Goudge et al., 2017; Horgan et al., 2020).

4.3. Implications for the early Martian atmosphere

Finally, an improved understanding of Fe(II)-carbonate mineralisation processes permits more robust atmospheric constraints derived from the rock record. Our experimental observations are consistent with geochemical studies of terrestrial aquatic environments (e.g., Postma, 1982) and CO₂ sequestration and storage (Gysi and Stefánsson, 2012) that indicate significant supersaturation states required for Fe(II)-carbonate formation, and this must be folded into future considerations of how carbonate-bearing deposits do or do not constrain atmospheric $p\text{CO}_2$. Our models show Fe(II)-carbonate is unlikely to form in a high water-rock ratio, open system even under high $p\text{CO}_2$, owing to how atmospherically controlled DIC contributions tend to outweigh the alkalinity generation from silicate mineral dissolution. This suggests that accurate palaeo- $p\text{CO}_2$ constraints may be difficult to derive from estimates of carbonate exposed at the surface (Edwards and Ehlmann, 2015), or from strictly thermodynamic constraints on carbonate precipitation (e.g., Bristow et al., 2017).

This geochemical scenario for subsurface carbonate formation is consistent with recent observations of carbonates dominantly associated with the largest impact craters (Wray et al., 2016; Michalski and Niles, 2010; Michalski et al., 2013). In addition, global groundwater models (Kite and Melwani Daswani, 2019) and oxygen escape rates and hydrogen isotope ratios (Heard and Kite, 2020) have been interpreted to reflect a potentially significant subsurface carbon reservoir. Nevertheless, ancient subsurface environments preserved within the Martian crust remain poorly sampled, and accordingly, should feature as priority targets for orbital and *in-situ* exploration missions.

5. CONCLUSIONS

Our experiments demonstrate that Fe(II)-carbonate precipitation is subject to strong kinetic control, which is consistent with the current data constraining the distribution of Fe(II)-carbonates within the Martian crusts. This is also quantitatively consistent with our geochemical modelling of different anoxic, aqueous systems. We consider, based on this research, that the apparent rarity of Fe(II)-carbonates preserved at the modern Martian surface, and perhaps carbonates in general, may be attributed to the following: a rarity of both deep subsurface exposures and the high saturation state required for their precipitation in low temperature water-rock systems, as opposed to low atmospheric $p\text{CO}_2$ during Mars' deep past. This data, in turn, informs future investigations of the early Martian C-cycle, which is likely to be further constrained by observations acquired by NASA's *Mars 2020* mission. For example, orbital investigations of the *Perseverance* landing site, Jezero Crater, reveal that regional geology may host carbonates that are relatively Fe-rich (e.g., Horgan et al., 2020). The presence of authigenic siderite preserved at Jezero, for example, may in turn offer broad constraints on maximum

Fe(II)-carbonate saturation state that could be refined through inverse modelling approaches of water-rock interaction and sedimentation. More broadly, localised concentrations of siderite could best express relatively high alkalinity, rock-dominated environments responsible for efficiently burying inorganic carbon within the early Martian subsurface.

ACKNOWLEDGEMENTS

This study was funded by the UK Research and Innovation's Natural Environmental Research Council as part of the Doctoral Training Partnership in Environmental Research at the University of Oxford (grant number NE/L002612/1). The authors wish to thank the insightful comments of Louis Derry, Edwin Kite, and an anonymous reviewer, which significantly improved the science of this manuscript. The authors also wish to thank Louis Derry for his editorial handling and interest in the research. LEK wishes to thank Andrew Matzen and Bernie Wood for generous assistance and use of laboratory facilities for fayalite synthesis; Kat Clayton for assistance with XRD; Robert Jacobs for assistance with BET; Gillian MacKinnon for assistance with ICP-OES; Phil Holdship for assistance with ICP-MS; and Jon Wade for assistance with SEM as well as many helpful discussions. This study also benefited from helpful discussions with Clancy Zhijian Jiang.

Experiment group name	Initial pH	Maximum duration	DIC concentrations	Initial $p\text{CO}_2$ at initial pH of 2 or 4	Water-rock ratio(s)	Fayalite-forsterite ratio(s)
Low water-rock	2 and 4	60 days	33.51 mmol/kg	1.0 bar	1:1, 1:10	Fa, 1:1 Fa/Fo
Fayalite-bearing	2 and 4	85 days	3.356, 16.79, and 33.51 mmol/kg	0.1, 0.5, 1.0 bar	1:500	Fa
Fayalite-and forsterite-bearing	2 and 4	85 days	3.356, 16.79, and 33.51 mmol/kg	0.1, 0.5, 1.0 bar	1:500	1:1 Fa/Fo, 1:9 Fa/Fo
Non-CO₂	2 and 4	8 days	Non	Non	1:200, 1:500	Fa

Table 1: Table detailing the categories of the 86 experiments conducted in this research.

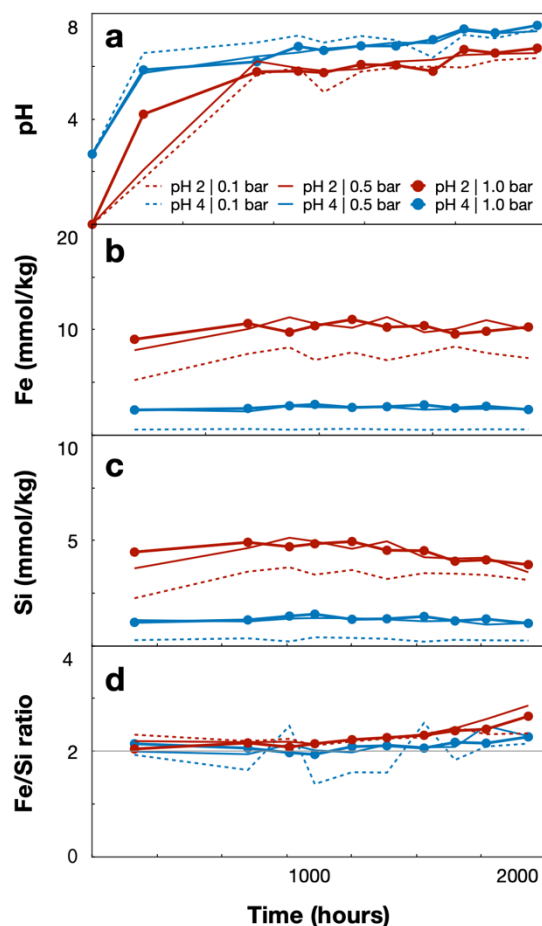


Figure 1: The pH, dissolved Fe and Si, and Fe/Si ratio over time through a typical fayalite-bearing experiment. Note the differing axes. (a) pH for experiments begun at pH 2 or 4, corresponding to equilibration with 0.1 to 1.0 bars of dissolved CO₂ at these initial pHs; (b) Fe concentration over time; (c) Si concentration over time; and (d) the ratio of Fe/Si over time, the stoichiometric ratio in pure fayalite marked as a grey line. Uncertainty for Fe and Si measurements is at 1.2 %; the uncertainty bars for this fall within the thickness of the lines. It is worth noting that $p\text{CO}_2$ depends on pH under a closed system and so will have fluctuated over the course of the experiments. Lines between datapoints are included for ease of following each dataset, and should not be construed as representing exact reaction pathway between datapoints.

[Single column image]

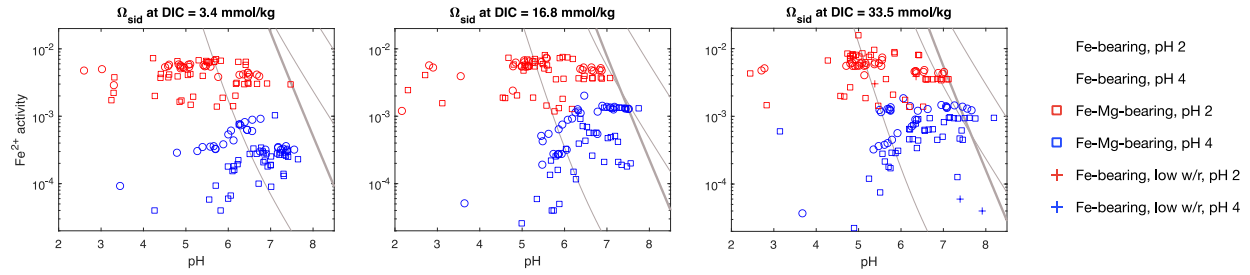


Figure 2: Fe^{2+} activity and pH from solution samples extracted at 10 intervals across 68 experiments, in separate graphs for Ω_{siderite} at DICs of 3.4, 16.8, and 33.5 mmol/kg. Datapoints in red correspond to experiments begun at pH 2; blue for pH 4. Circular datapoints correspond to fayalite-bearing experiments, while squares denote those bearing fayalite and forsterite, and plus-symbols for low water:rock ratio (1:10). pH and Fe^{2+} activity generally increased over the course of an experiment, thus datapoints towards the upper-right generally correspond to increasing reaction times. From left to right, the thin grey lines denote contours of Ω_{siderite} : 1, 400, and 5000. The heavy grey line is the AFC saturation line of Jiang and Tosca (2019).

[Double column image]

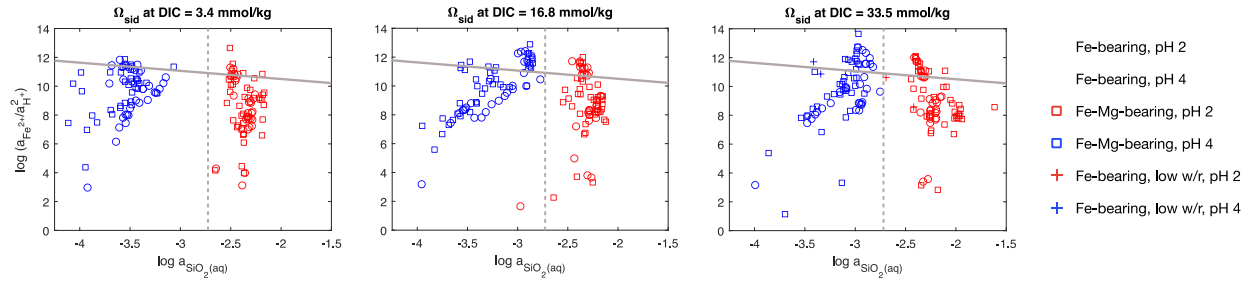


Figure 3: Solubility diagrams for the Fe(II)-silicate system involving the three principal factors controlling greenalite stability. All data are from solution samples extracted at 10 intervals across 68 experiments. Datapoints in red correspond to experiments begun at pH 2; blue for pH 4. Circular datapoints correspond to fayalite-bearing experiments, while squares denote those bearing fayalite and forsterite, and plus-symbols for low water:rock ratio (1:10). Datapoints towards the upper-right generally correspond to increasing reaction times. The heavy grey corresponds to the greenalite saturation (Tosca et al., 2016). The dashed grey line corresponds to amorphous silica saturation (Siever 1992).

[Double column image]

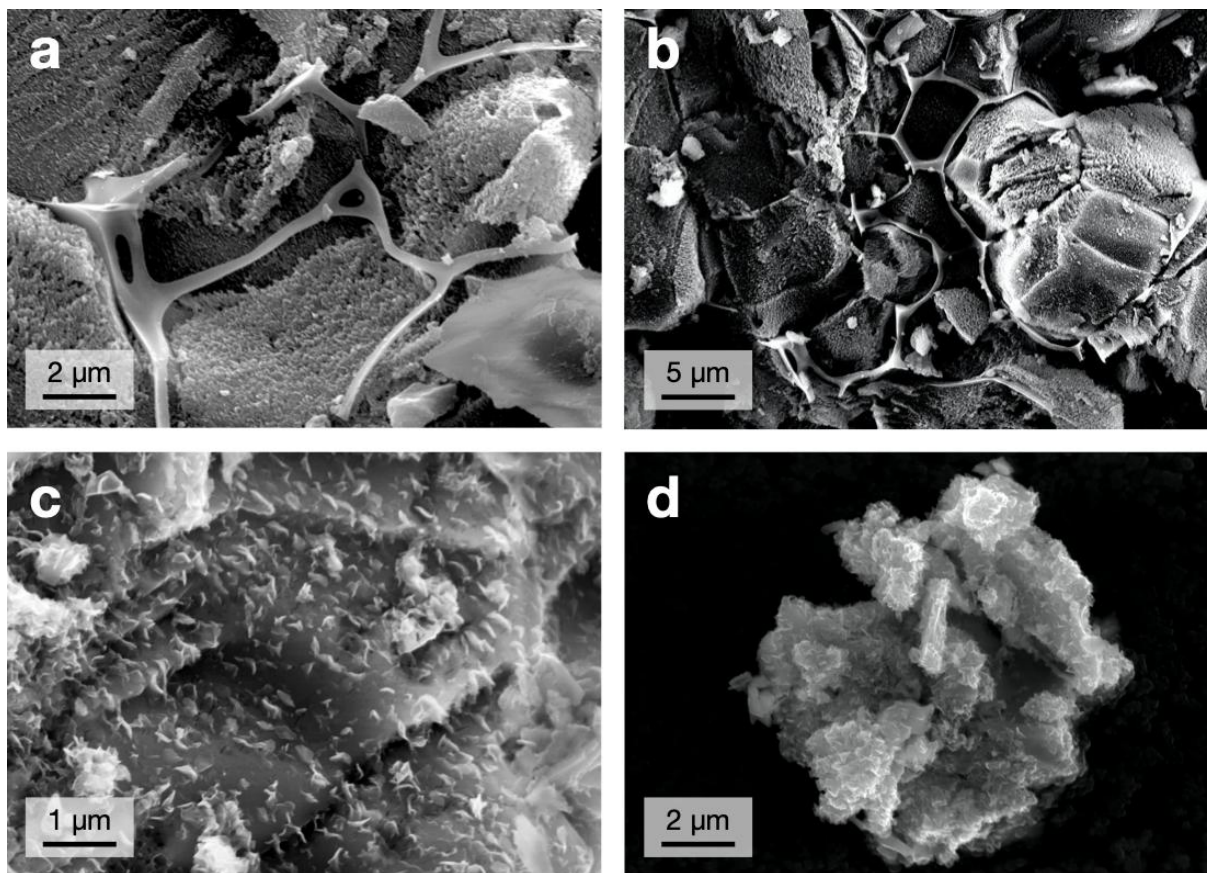


Figure 4: (a) Long, thin, fibrous structures found only upon or between (b) fayalite grains, apparently growing in interstitial spaces and breaking loose when disturbed, as in (a). (c) Aligned, nanometre-scaled precipitates found only upon fayalite grains, or (d) either as individual nuclei apparently formed of the precipitates' coalescence and growth upon each other, or growth upon a separate aggregate.

[Double column image]

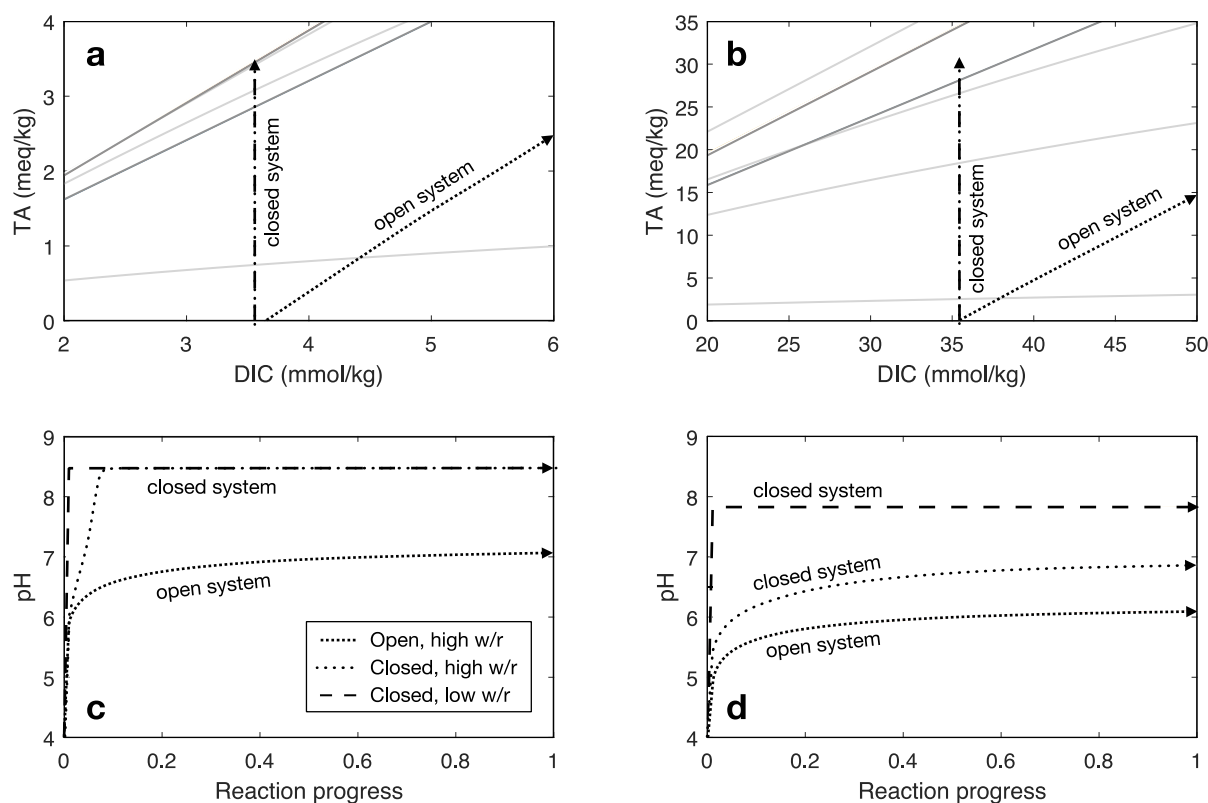


Figure 5: Results from three reaction path models of water-rock interaction at 25 °C: open-system with respect to CO₂ at high water:rock ratio (tightly-dotted lines), closed-system with respect to CO₂ at high water:rock ratio (circular-dotted lines), and closed-system with respect to CO₂ at low water:rock ratio (dashed lines). Left column: models run with 0.1 bar CO₂; right column: models run with 1.0 bar CO₂. (a) and (b): siderite and AFC saturation state as a function of DIC and total alkalinity (TA). From bottom-up, pale-grey lines represent Ω_{siderite} of 1, 100, 400, and 100,000; from bottom-up, dark-grey lines represent an Ω_{AFC} saturation at pH 7 (lower) or 8 (higher). (c) and (d): pH variation over the course of the experiment (which corresponds closely to total alkalinity in this system). In order to illustrate the influence of water-rock interaction on the Fe(II)-carbonate system in DIC-TA space, these models were run under fixed Fe²⁺ concentration of 10 mmol/kg with forsterite as the sole reactant.

[Double column image]

670 REFERENCES

- 671 Aagaard, P., Helgeson, H.C., 1982. Thermodynamic and kinetic constraints on reaction rates
 672 among minerals and aqueous solutions; I, Theoretical considerations. *Am. J. Sci.* 282,
 673 237–285. <https://doi.org/10.2475/ajs.282.3.237>
- 674 Bandfield, J.L., Glotch, T.D., Christensen, P.R., 2003. Spectroscopic Identification of Carbonate
 675 Minerals in the Martian Dust. *Science* 301, 1084–1087.
 676 <https://doi.org/10.1126/science.1088054>
- 677 Bandstra, J.Z., Brantley, S.L., 2008. Data Fitting Techniques with Applications to Mineral
 678 Dissolution Kinetics, in: Brantley, S.L., Kubicki, J.D., White, A.F. (Eds.), *Kinetics of*
 679 *Water-Rock Interaction*. Springer New York, New York, NY, pp. 211–257.
 680 https://doi.org/10.1007/978-0-387-73563-4_6
- 681 Bethke, C.M., 2017. *The Geochemist's Workbench, Version 12.0: GWB Essentials Guide*.
 682 Champaign, Illinois, US.
- 683 Boynton, W.V., Ming, D.W., Kounaves, S.P., Young, S.M.M., Arvidson, R.E., Hecht, M.H.,
 684 Hoffman, J., Niles, P.B., Hamara, D.K., Quinn, R.C., Smith, P.H., Sutter, B., Catling,
 685 D.C., Morris, R.V., 2009. Evidence for Calcium Carbonate at the Mars Phoenix Landing
 686 Site. *Science* 325, 61–64. <https://doi.org/10.1126/science.1172768>
- 687 Brantley, S.L., Mellott, N.P., 2000. Surface area and porosity of primary silicate minerals. *Am.*
 688 *Mineral.* 85, 1767–1783. <https://doi.org/10.2138/am-2000-11-1220>
- 689 Braterman, P.S., Graham Cairns-Smith, A., W. Sloper, R., George Truscott, T., Craw, M., 1984.
 690 Photo-oxidation of iron(II) in water between pH 7.5 and 4.0. *J. Chem. Soc. Dalton*
 691 *Trans.* 0, 1441–1445. <https://doi.org/10.1039/DT9840001441>
- 692 Bridges, J.C., Catling, D.C., Saxton, J.M., Swindle, T.D., Lyon, I.C., Grady, M.M., 2001.
 693 Alteration Assemblages in Martian Meteorites: Implications for Near-Surface Processes.
 694 *Space Sci. Rev.* 96, 365–392. <https://doi.org/10.1023/A:1011965826553>
- 695 Bridges, J.C., Hicks, L.J., Treiman, A.H., 2019. Carbonates on Mars, in: *Volatiles in the Martian*
 696 *Crust*. Elsevier, pp. 89–118. <https://doi.org/10.1016/B978-0-12-804191-8.00005-2>
- 697 Bristow, T.F., Haberle, R.M., Blake, D.F., Marais, D.J.D., Eigenbrode, J.L., Fairén, A.G.,
 698 Grotzinger, J.P., Stack, K.M., Mischna, M.A., Rampe, E.B., Siebach, K.L., Sutter, B.,
 699 Vaniman, D.T., Vasavada, A.R., 2017. Low Hesperian PCO₂ constrained from in situ
 700 mineralogical analysis at Gale Crater, Mars. *Proc. Natl. Acad. Sci.* 201616649.
 701 <https://doi.org/10.1073/pnas.1616649114>
- 702 Brown, A.J., Viviano, C.E., Goudge, T.A., 2020. Olivine- Carbonate Mineralogy of the Jezero
 703 Crater Region. *J. Geophys. Res. Planets* 125. <https://doi.org/10.1029/2019JE006011>
- 704 Butler, I.B., Schoonen, M.A.A., Rickard, D.T., 1994. Removal of dissolved oxygen from water:
 705 A comparison of four common techniques. *Talanta* 41, 211–215.
 706 [https://doi.org/10.1016/0039-9140\(94\)80110-X](https://doi.org/10.1016/0039-9140(94)80110-X)
- 707 Delany, J.M., Lundeen, S.R., 1991. The LLNL thermochemical data base--revised data and file
 708 format for the EQ3/6 package. Lawrence Livermore National Lab., CA (United States).
 709 Vancouver.
- 710 Edwards, C.S., Ehlmann, B.L., 2015. Carbon sequestration on Mars. *Geology* 43, 863–866.
 711 <https://doi.org/10.1130/G36983.1>
- 712 Ehlmann, B.L., Bish, D.L., Ruff, S.W., Mustard, J.F., 2012. Mineralogy and chemistry of altered
 713 Icelandic basalts: Application to clay mineral detection and understanding aqueous

environments on Mars: CLAY MINERAL DETECTION, ICELANDIC BASALT. *J. Geophys. Res. Planets* 117, n/a-n/a. <https://doi.org/10.1029/2012JE004156>

Ehlmann, B.L., Mustard, J.F., Murchie, S.L., Poulet, F., Bishop, J.L., Brown, A.J., Calvin, W.M., Clark, R.N., Marais, D.J.D., Milliken, R.E., Roach, L.H., Roush, T.L., Swayze, G.A., Wray, J.J., 2008. Orbital Identification of Carbonate-Bearing Rocks on Mars. *Science* 322, 1828–1832. <https://doi.org/10.1126/science.1164759>

Fairén, A.G., Fernández-Remolar, D., Dohm, J.M., Baker, V.R., Amils, R., 2004. Inhibition of carbonate synthesis in acidic oceans on early Mars. *Nature* 431, 423–426. <https://doi.org/10.1038/nature02911>

Farmer, V.C. (Ed.), 1974. *The Infrared Spectra of Minerals*. Mineralogical Society of Great Britain and Ireland, London. <https://doi.org/10.1180/mono-4>

Feitknecht, W., Schindler, P., 1963. Solubility constants of metal oxides, metal hydroxides and metal hydroxide salts in aqueous solution. *Pure Appl. Chem.* 6, 125–206. <https://doi.org/10.1351/pac196306020125>

Gislason, S.R., Arnorsson, S., Armannsson, H., 1996. Chemical weathering of basalt in Southwest Iceland; effects of runoff, age of rocks and vegetative/glacial cover. *Am. J. Sci.* 296, 837–907. <https://doi.org/10.2475/ajs.296.8.837>

Gysi, A.P., Stefánsson, A., 2012. CO₂-water-basalt interaction. Low temperature experiments and implications for CO₂ sequestration into basalts. *Geochim. Cosmochim. Acta* 81, 129–152. <https://doi.org/10.1016/j.gca.2011.12.012>

Halevy, I., Fischer, W.W., Eiler, J.M., 2011. Carbonates in the Martian meteorite Allan Hills 84001 formed at 18 ± 4 °C in a near-surface aqueous environment. *Proc. Natl. Acad. Sci.* 108, 16895–16899. <https://doi.org/10.1073/pnas.1109444108>

He, S., Morse, J.W., 1993. The carbonic acid system and calcite solubility in aqueous Na-K-Ca-Mg-Cl-SO₄ solutions from 0 to 90°C. *Geochim. Cosmochim. Acta* 57, 3533–3554. [https://doi.org/10.1016/0016-7037\(93\)90137-L](https://doi.org/10.1016/0016-7037(93)90137-L)

Heard, A.W., Kite, E.S., 2020. A probabilistic case for a large missing carbon sink on Mars after 3.5 billion years ago. *Earth Planet. Sci. Lett.* 531, 116001. <https://doi.org/10.1016/j.epsl.2019.116001>

Helgeson, H.C., Kirkham, D.H., 1974. Theoretical prediction of the thermodynamic behavior of aqueous electrolytes at high pressures and temperatures; II, Debye-Huckel parameters for activity coefficients and relative partial molal properties. *Am. J. Sci.* 274, 1199–1261. <https://doi.org/10.2475/ajs.274.10.1199>

Horgan, B.H.N., Anderson, R.B., Dromart, G., Amador, E.S., Rice, M.S., 2020. The mineral diversity of Jezero crater: Evidence for possible lacustrine carbonates on Mars. *Icarus* 339, 113526. <https://doi.org/10.1016/j.icarus.2019.113526>

Hurowitz, J.A., Fischer, W.W., Tosca, N.J., Milliken, R.E., 2010. Origin of acidic surface waters and the evolution of atmospheric chemistry on early Mars. *Nat. Geosci.* 3, 323–326. <https://doi.org/10.1038/ngeo831>

Hurowitz, J.A., Grotzinger, J.P., Fischer, W.W., McLennan, S.M., Milliken, R.E., Stein, N., Vasavada, A.R., Blake, D.F., Dehouck, E., Eigenbrode, J.L., Fairén, A.G., Frydenvang, J., Gellert, R., Grant, J.A., Gupta, S., Herkenhoff, K.E., Ming, D.W., Rampe, E.B., Schmidt, M.E., Siebach, K.L., Stack-Morgan, K., Sumner, D.Y., Wiens, R.C., 2017. Redox stratification of an ancient lake in Gale crater, Mars. *Science* 356, eaah6849. <https://doi.org/10.1126/science.aah6849>

- Jakosky, B.M., 2019. The CO₂ inventory on Mars. *Planet. Space Sci.* 175, 52–59.
<https://doi.org/10.1016/j.pss.2019.06.002>
- Jiang, C.Z., Tosca, N.J., 2020. Growth kinetics of siderite at 298.15 K and 1 bar. *Geochim. Cosmochim. Acta* 274, 97–117. <https://doi.org/10.1016/j.gca.2020.01.047>
- Jiang, C.Z., Tosca, N.J., 2019. Fe(II)-carbonate precipitation kinetics and the chemistry of anoxic ferruginous seawater. *Earth Planet. Sci. Lett.* 506, 231–242.
<https://doi.org/10.1016/j.epsl.2018.11.010>
- Jimenez-Lopez, C., Romanek, C.S., 2004. Precipitation kinetics and carbon isotope partitioning of inorganic siderite at 25°C and 1 atm. *Geochim. Cosmochim. Acta* 68, 557–571.
[https://doi.org/10.1016/S0016-7037\(03\)00460-5](https://doi.org/10.1016/S0016-7037(03)00460-5)
- Kashchiev, D., Verdoes, D., van Rosmalen, G.M., 1991. Induction time and metastability limit in new phase formation. *J. Cryst. Growth* 110, 373–380. [https://doi.org/10.1016/0022-0248\(91\)90273-8](https://doi.org/10.1016/0022-0248(91)90273-8)
- Kite, E.S., Melwani Daswani, M., 2019. Geochemistry constrains global hydrology on Early Mars. *Earth Planet. Sci. Lett.* 524, 115718. <https://doi.org/10.1016/j.epsl.2019.115718>
- Kling, A.M., Haberle, R.M., McKay, C.P., Bristow, T.F., Rivera-Hernández, F., 2020. Subsistence of ice-covered lakes during the Hesperian at Gale crater, Mars. *Icarus* 338, 113495. <https://doi.org/10.1016/j.icarus.2019.113495>
- Königsberger, E., Königsberger, L.-C., Gamsjäger, H., 1999. Low-temperature thermodynamic model for the system Na₂CO₃–MgCO₃–CaCO₃–H₂O. *Geochim. Cosmochim. Acta* 63, 3105–3119. [https://doi.org/10.1016/S0016-7037\(99\)00238-0](https://doi.org/10.1016/S0016-7037(99)00238-0)
- Lasaga, A.C., 1998. *Kinetic Theory in the Earth Sciences*. Princeton University Press, Princeton.
<https://doi.org/10.1515/9781400864874>
- Malin, M.C., Edgett, K.S., 2000. Sedimentary Rocks of Early Mars. *Science* 290, 1927–1937.
<https://doi.org/10.1126/science.290.5498.1927>
- McLennan, S.M., Grotzinger, J.P., Hurowitz, J.A., Tosca, N.J., 2019. The Sedimentary Cycle on Early Mars. *Annu. Rev. Earth Planet. Sci.* 47, 91–118. <https://doi.org/10.1146/annurev-earth-053018-060332>
- Michalski, J.R., Cuadros, J., Bishop, J.L., Darby Dyar, M., Dekov, V., Fiore, S., 2015. Constraints on the crystal-chemistry of Fe/Mg-rich smectitic clays on Mars and links to global alteration trends. *Earth Planet. Sci. Lett.* 427, 215–225.
<https://doi.org/10.1016/j.epsl.2015.06.020>
- Michalski, J.R., Cuadros, J., Niles, P.B., Parnell, J., Deanne Rogers, A., Wright, S.P., 2013. Groundwater activity on Mars and implications for a deep biosphere. *Nat. Geosci.* 6, 133–138. <https://doi.org/10.1038/ngeo1706>
- Michalski, J.R., Niles, P.B., 2010. Deep crustal carbonate rocks exposed by meteor impact on Mars. *Nat. Geosci.* 3, 751–755. <https://doi.org/10.1038/ngeo971>
- Milliken, R.E., Fischer, W.W., Hurowitz, J.A., 2009. Missing salts on early Mars. *Geophys. Res. Lett.* 36, L11202. <https://doi.org/10.1029/2009GL038558>
- Ming, D.W., Archer, P.D., Glavin, D.P., Eigenbrode, J.L., Franz, H.B., Sutter, B., Brunner, A.E., Stern, J.C., Freissinet, C., McAdam, A.C., Mahaffy, P.R., Cabane, M., Coll, P., Campbell, J.L., Atreya, S.K., Niles, P.B., Bell, J.F., Bish, D.L., Brinckerhoff, W.B., Buch, A., Conrad, P.G., Des Marais, D.J., Ehlmann, B.L., Fairen, A.G., Farley, K., Flesch, G.J., Francois, P., Gellert, R., Grant, J.A., Grotzinger, J.P., Gupta, S., Herkenhoff, K.E., Hurowitz, J.A., Leshin, L.A., Lewis, K.W., McLennan, S.M., Miller, K.E., Moersch, J., Morris, R.V., Navarro-Gonzalez, R., Pavlov, A.A., Perrett, G.M., Pradler, I.,

805 Squyres, S.W., Summons, R.E., Steele, A., Stolper, E.M., Sumner, D.Y., Szopa, C.,
806 Teinturier, S., Trainer, M.G., Treiman, A.H., Vaniman, D.T., Vasavada, A.R., Webster,
807 C.R., Wray, J.J., Yingst, R.A., MSL Science Team, Kemppinen, O., Bridges, N.,
808 Johnson, J.R., Minitti, M., Cremers, D., Edgar, L., Farmer, J., Godber, A., Wadhwa, M.,
809 Wellington, D., McEwan, I., Newman, C., Richardson, M., Charpentier, A., Peret, L.,
810 King, P., Blank, J., Weigle, G., Schmidt, M., Li, S., Milliken, R., Robertson, K., Sun, V.,
811 Baker, M., Edwards, C., Ehlmann, B., Griffes, J., Newcombe, M., Pilorget, C., Rice, M.,
812 Siebach, K., Stack, K., Brunet, C., Hipkin, V., Leveille, R., Marchand, G., Sanchez, P.S.,
813 Favot, L., Cody, G., Fluckiger, L., Lees, D., Nefian, A., Martin, M., Gailhanou, M.,
814 Westall, F., Israel, G., Agard, C., Baroukh, J., Donny, C., Gaboriaud, A., Guillemot, P.,
815 Lafaille, V., Lorigny, E., Paillet, A., Perez, R., Saccoccio, M., Yana, C., Armiens-
816 Aparicio, C., Rodriguez, J.C., Blazquez, I.C., Gomez, F.G., Gomez-Elvira, J., Hettrich,
817 S., Malvitte, A.L., Jimenez, M.M., Martinez-Frias, J., Martin-Soler, J., Martin-Torres,
818 F.J., Jurado, A.M., Mora-Sotomayor, L., Caro, G.M., Lopez, S.N., Peinado-Gonzalez, V.,
819 Pla-Garcia, J., Manfredi, J.A.R., Romeral-Planello, J.J., Fuentes, S.A.S., Martinez, E.S.,
820 Redondo, J.T., Urqui-O'Callaghan, R., Mier, M.-P.Z., Chipera, S., Lacour, J.-L.,
821 Mauchien, P., Sirven, J.-B., Manning, H., Hayes, A., Joseph, J., Sullivan, R., Thomas, P.,
822 Dupont, A., Lundberg, A., Melikechi, N., Mezzacappa, A., DeMarines, J., Grinspoon, D.,
823 Reitz, G., Prats, B., Atlaskin, E., Genzer, M., Harri, A.-M., Haukka, H., Kahanpaa, H.,
824 Kauhanen, J., Kemppinen, O., Paton, M., Polkko, J., Schmidt, W., Siili, T., Fabre, C.,
825 Wilhelm, M.B., Poitrasson, F., Patel, K., Gorevan, S., Indyk, S., Paulsen, G., Schieber, J.,
826 Gondet, B., Langevin, Y., Geffroy, C., Baratoux, D., Berger, G., Cros, A., d'Uston, C.,
827 Forni, O., Gasnault, O., Lasue, J., Lee, Q.-M., Maurice, S., Meslin, P.-Y., Pallier, E.,
828 Parot, Y., Pinet, P., Schroder, S., Toplis, M., Lewin, E., Brunner, W., Heydari, E.,
829 Achilles, C., Oehler, D., Coscia, D., Israel, G., Dromart, G., Robert, F., Sautter, V., Le
830 Mouelic, S., Mangold, N., Nachon, M., Stalport, F., Raulin, F., Cameron, J., Clegg, S.,
831 Cousin, A., DeLapp, D., Dingler, R., Jackson, R.S., Johnstone, S., Lanza, N., Little, C.,
832 Nelson, T., Wiens, R.C., Williams, R.B., Jones, A., Kirkland, L., Baker, B., Cantor, B.,
833 Caplinger, M., Davis, S., Duston, B., Edgett, K., Fay, D., Hardgrove, C., Harker, D.,
834 Herrera, P., Jensen, E., Kennedy, M.R., Krezoski, G., Krysak, D., Lipkaman, L., Malin,
835 M., McCartney, E., McNair, S., Nixon, B., Posiolova, L., Ravine, M., Salamon, A.,
836 Saper, L., Stoiber, K., Supulver, K., Van Beek, J., Van Beek, T., Zimdar, R., French,
837 K.L., Iagnemma, K., Miller, K., Goesmann, F., Goetz, W., Hviid, S., Johnson, M.,
838 Lefavor, M., Lyness, E., Breves, E., Dyar, M.D., Fassett, C., Blake, D.F., Bristow, T.,
839 Edwards, L., Haberle, R., Hoehler, T., Hollingsworth, J., Kahre, M., Keely, L., McKay,
840 C., Wilhelm, M.B., Bleacher, L., Choi, D., Dworkin, J.P., Floyd, M., Garvin, J., Harpold,
841 D., Jones, A., Martin, D.K., Raaen, E., Smith, M.D., Tan, F., Meyer, M., Posner, A.,
842 Voytek, M., Anderson, R.C., Aubrey, A., Beegle, L.W., Behar, A., Blaney, D., Brinza,
843 D., Calef, F., Christensen, L., Crisp, J.A., DeFlores, L., Feldman, J., Feldman, S., Jun, I.,
844 Keymeulen, D., Maki, J., Mischna, M., Morookian, J.M., Parker, T., Pavri, B.,
845 Schoppers, M., Sengstacken, A., Simmonds, J.J., Spanovich, N., Juarez, M. d. I. T., Yen,
846 A., Cucinotta, F., Jones, J.H., Rampe, E., Nolan, T., Fisk, M., Radziemski, L.,
847 Barraclough, B., Bender, S., Berman, D., Dobra, E.N., Tokar, R., Williams, R.M.E.,
848 Cleghorn, T., Huntress, W., Manhes, G., Hudgins, J., Olson, T., Stewart, N., Sarrazin, P.,
849 Vicenzi, E., Wilson, S.A., Bullock, M., Ehresmann, B., Hamilton, V., Hassler, D.,
850 Peterson, J., Rafkin, S., Zeitlin, C., Fedosov, F., Golovin, D., Karpushkina, N., Kozyrev,

A., Litvak, M., Malakhov, A., Mitrofanov, I., Mokrousov, M., Nikiforov, S., Prokhorov, V., Sanin, A., Tretyakov, V., Varenikov, A., Vostrukhin, A., Kuzmin, R., Clark, B., Wolff, M., Botta, O., Drake, D., Bean, K., Lemmon, M., Schwenzer, S.P., Anderson, R.B., Lee, E.M., Sucharski, R., Hernandez, M.A. d. P., Avalos, J.J.B., Ramos, M., Kim, M.-H., Malespin, C., Plante, I., Muller, J.-P., Ewing, R., Boynton, W., Downs, R., Fitzgibbon, M., Harshman, K., Morrison, S., Dietrich, W., Kortmann, O., Palucis, M., Williams, A., Lugmair, G., Wilson, M.A., Rubin, D., Jakosky, B., Balic-Zunic, T., Frydenvang, J., Jensen, J.K., Kinch, K., Koefoed, A., Madsen, M.B., Stipp, S.L.S., Boyd, N., VanBommel, S., Jacob, S., Owen, T., Rowland, S., Atlaskin, E., Savijarvi, H., Boehm, E., Bottcher, S., Burmeister, S., Guo, J., Kohler, J., Garcia, C.M., Mueller-Mellin, R., Wimmer-Schweingruber, R., Bridges, J.C., McConnochie, T., Benna, M., Bower, H., Blau, H., Boucher, T., Carmosino, M., Elliott, H., Halleaux, D., Renno, N., Wong, M., Pepin, R., Elliott, B., Spray, J., Thompson, L., Gordon, S., Newsom, H., Ollila, A., Williams, J., Vasconcelos, P., Bentz, J., Nealson, K., Popa, R., Kah, L.C., Tate, C., Day, M., Kocurek, G., Hallet, B., Sletten, R., Francis, R., McCullough, E., Cloutis, E., ten Kate, I.L., Kuzmin, R., Arvidson, R., Fraeman, A., Scholes, D., Slavney, S., Stein, T., Ward, J., Berger, J., Moores, J.E., 2014. Volatile and Organic Compositions of Sedimentary Rocks in Yellowknife Bay, Gale Crater, Mars. *Science* 343, 1245267–1245267. <https://doi.org/10.1126/science.1245267>

Morris, R.V., Ruff, S.W., Gellert, R., Ming, D.W., Arvidson, R.E., Clark, B.C., Golden, D.C., Siebach, K., Klingelhofer, G., Schroder, C., Fleischer, I., Yen, A.S., Squyres, S.W., 2010. Identification of Carbonate-Rich Outcrops on Mars by the Spirit Rover. *Science* 329, 421–424. <https://doi.org/10.1126/science.1189667>

Nordstrom, D.K., 1977. Thermochemical redox equilibria of ZoBell's solution. *Geochim. Cosmochim. Acta* 41, 1835–1841. [https://doi.org/10.1016/0016-7037\(77\)90215-0](https://doi.org/10.1016/0016-7037(77)90215-0)

Oelkers, E.H., Golubev, S.V., Chairat, C., Pokrovsky, O.S., Schott, J., 2009. The surface chemistry of multi-oxide silicates. *Geochim. Cosmochim. Acta* 73, 4617–4634. <https://doi.org/10.1016/j.gca.2009.05.028>

Owen, T., Biemann, K., Rushneck, D.R., Biller, J.E., Howarth, D.W., Lafleur, A.L., 1977. The composition of the atmosphere at the surface of Mars. *J. Geophys. Res.* 82, 4635–4639. <https://doi.org/10.1029/JS082i028p04635>

Perez-Fodich, A., Derry, L.A., 2019. Organic acids and high soil CO₂ drive intense chemical weathering of Hawaiian basalts: Insights from reactive transport models. *Geochim. Cosmochim. Acta* 249, 173–198. <https://doi.org/10.1016/j.gca.2019.01.027>

Pokrovsky, O.S., Schott, J., 2000. Forsterite surface composition in aqueous solutions: a combined potentiometric, electrokinetic, and spectroscopic approach. *Geochim. Cosmochim. Acta* 64, 3299–3312. [https://doi.org/10.1016/S0016-7037\(00\)00435-X](https://doi.org/10.1016/S0016-7037(00)00435-X)

Pollack, J.B., Kasting, J.F., Richardson, S.M., Poliakov, K., 1987. The case for a wet, warm climate on early Mars. *Icarus* 71, 203–224. [https://doi.org/10.1016/0019-1035\(87\)90147-3](https://doi.org/10.1016/0019-1035(87)90147-3)

Postma, D., 1982. Pyrite and siderite formation in brackish and freshwater swamp sediments. *Am. J. Sci.* 282, 1151–1183. <https://doi.org/10.2475/ajs.282.8.1151>

Power, I.M., Harrison, A.L., Dipple, G.M., Wilson, S.A., Barker, S.L.L., Fallon, S.J., 2019. Magnesite formation in playa environments near Atlin, British Columbia, Canada. *Geochim. Cosmochim. Acta* 255, 1–24. <https://doi.org/10.1016/j.gca.2019.04.008>

- Qafoku, O., Kovarik, L., Kukkadapu, R.K., Ilton, E.S., Arey, B.W., Tucek, J., Felmy, A.R., 2012. Fayalite dissolution and siderite formation in water-saturated supercritical CO₂. *Chem. Geol.* 332–333, 124–135. <https://doi.org/10.1016/j.chemgeo.2012.09.028>
- Ruff, S.W., Niles, P.B., Alfano, F., Clarke, A.B., 2014. Evidence for a Noachian-aged ephemeral lake in Gusev crater, Mars. *Geology* 42, 359–362. <https://doi.org/10.1130/G35508.1>
- Siever, R., 1992. The silica cycle in the Precambrian. *Geochim. Cosmochim. Acta* 56, 3265–3272. [https://doi.org/10.1016/0016-7037\(92\)90303-Z](https://doi.org/10.1016/0016-7037(92)90303-Z)
- Singer, P.C., Stumm, W., 1970. The Solubility of Ferrous Iron in Carbonate-Bearing Waters. *J. - Am. Water Works Assoc.* 62, 198–202. <https://doi.org/10.1002/j.1551-8833.1970.tb03888.x>
- Stein, N., Grotzinger, J.P., Schieber, J., Mangold, N., Hallet, B., Newsom, H., Stack, K.M., Berger, J.A., Thompson, L., Siebach, K.L., Cousin, A., Le Mouélic, S., Minitti, M., Sumner, D.Y., Fedo, C., House, C.H., Gupta, S., Vasavada, A.R., Gellert, R., Wiens, R.C., Frydenvang, J., Forni, O., Meslin, P.Y., Payré, V., Dehouck, E., 2018. Desiccation cracks provide evidence of lake drying on Mars, Sutton Island member, Murray formation, Gale Crater. *Geology* 46, 515–518. <https://doi.org/10.1130/G40005.1>
- Tosca, N.J., Ahmed, I.A.M., Tutolo, B.M., Ashpitel, A., Hurowitz, J.A., 2018. Magnetite authigenesis and the warming of early Mars. *Nat. Geosci.* 11, 635–639. <https://doi.org/10.1038/s41561-018-0203-8>
- Tosca, N.J., Guggenheim, S., Pufahl, P.K., 2016. An authigenic origin for Precambrian greenalite: Implications for iron formation and the chemistry of ancient seawater. *Geol. Soc. Am. Bull.* 128, 511–530. <https://doi.org/10.1130/B31339.1>
- Turnbull, D., Fisher, J.C., 1949. Rate of Nucleation in Condensed Systems. *J. Chem. Phys.* 17, 71–73. <https://doi.org/10.1063/1.1747055>
- Vagenas, N., Gatsouli, A., Kontoyannis, C.G., 2003. Quantitative analysis of synthetic calcium carbonate polymorphs using FT-IR spectroscopy. *Talanta* 59, 831–836. [https://doi.org/10.1016/S0039-9140\(02\)00638-0](https://doi.org/10.1016/S0039-9140(02)00638-0)
- van Berk, W., Fu, Y., 2011. Reproducing hydrogeochemical conditions triggering the formation of carbonate and phyllosilicate alteration mineral assemblages on Mars (Nili Fossae region). *J. Geophys. Res.* 116, E10006. <https://doi.org/10.1029/2011JE003886>
- Vaniman, D.T., Bish, D.L., Ming, D.W., Bristow, T.F., Morris, R.V., Blake, D.F., Chipera, S.J., Morrison, S.M., Treiman, A.H., Rampe, E.B., Rice, M., Achilles, C.N., Grotzinger, J.P., McLennan, S.M., Williams, J., Bell, J.F., Newsom, H.E., Downs, R.T., Maurice, S., Sarrazin, P., Yen, A.S., Morookian, J.M., Farmer, J.D., Stack, K., Milliken, R.E., Ehlmann, B.L., Sumner, D.Y., Berger, G., Crisp, J.A., Hurowitz, J.A., Anderson, R., Des Marais, D.J., Stolper, E.M., Edgett, K.S., Gupta, S., Spanovich, N., MSL Science Team, Agard, C., Alves Verdasca, J.A., Anderson, R., Archer, D., Armiens-Aparicio, C., Arvidson, R., Ataskin, E., Atreya, S., Aubrey, A., Baker, B., Baker, M., Balic-Zunic, T., Baratoux, D., Baroukh, J., Barraclough, B., Bean, K., Beegle, L., Behar, A., Bender, S., Benna, M., Bentz, J., Berger, J., Berman, D., Blanco Avalos, J.J., Blaney, D., Blank, J., Blau, H., Bleacher, L., Boehm, E., Botta, O., Bottcher, S., Boucher, T., Bower, H., Boyd, N., Boynton, B., Breves, E., Bridges, J., Bridges, N., Brinckerhoff, W., Brinza, D., Brunet, C., Brunner, A., Brunner, W., Buch, A., Bullock, M., Burmeister, S., Cabane, M., Calef, F., Cameron, J., Campbell, J.I., Cantor, B., Caplinger, M., Caride Rodriguez, J., Carmosino, M., Carrasco Blazquez, I., Charpentier, A., Choi, D., Clark, B., Clegg, S., Cleghorn, T., Cloutis, E., Cody, G., Coll, P., Conrad, P., Coscia, D., Cousin, A., Cremers,

942 D., Cros, A., Cucinotta, F., d'Uston, C., Davis, S., Day, M.K., de la Torre Juarez, M.,
 943 DeFlores, L., DeLapp, D., DeMarines, J., Dietrich, W., Dingler, R., Donny, C., Drake,
 944 D., Dromart, G., Dupont, A., Duston, B., Dworkin, J., Dyar, M.D., Edgar, L., Edwards,
 945 C., Edwards, L., Ehresmann, B., Eigenbrode, J., Elliott, B., Elliott, H., Ewing, R., Fabre,
 946 C., Fairen, A., Farley, K., Fassett, C., Favot, L., Fay, D., Fedosov, F., Feldman, J.,
 947 Feldman, S., Fisk, M., Fitzgibbon, M., Flesch, G., Floyd, M., Fluckiger, L., Forni, O.,
 948 Fraeman, A., Francis, R., Francois, P., Franz, H., Freissinet, C., French, K.L.,
 949 Frydenvang, J., Gaboriaud, A., Gailhanou, M., Garvin, J., Gasnault, O., Geffroy, C.,
 950 Gellert, R., Genzer, M., Glavin, D., Godber, A., Goesmann, F., Goetz, W., Golovin, D.,
 951 Gomez Gomez, F., Gomez-Elvira, J., Gondet, B., Gordon, S., Gorevan, S., Grant, J.,
 952 Griffes, J., Grinspoon, D., Guillemot, P., Guo, J., Guzewich, S., Haberle, R., Halleaux,
 953 D., Hallet, B., Hamilton, V., Hardgrove, C., Harker, D., Harpold, D., Harri, A.-M.,
 954 Harshman, K., Hassler, D., Haukka, H., Hayes, A., Herkenhoff, K., Herrera, P., Hettrich,
 955 S., Heydari, E., Hipkin, V., Hoehler, T., Hollingsworth, J., Hudgins, J., Huntress, W.,
 956 Hviid, S., Iagnemma, K., Indyk, S., Israel, G., Jackson, R., Jacob, S., Jakosky, B., Jensen,
 957 E., Jensen, J.K., Johnson, J., Johnson, M., Johnstone, S., Jones, A., Jones, J., Joseph, J.,
 958 Jun, I., Kah, L., Kahanpaa, H., Kahre, M., Karpushkina, N., Kasprzak, W., Kauhanen, J.,
 959 Keely, L., Kemppinen, O., Keymeulen, D., Kim, M.-H., Kinch, K., King, P., Kirkland,
 960 L., Kocurek, G., Koefoed, A., Kohler, J., Kortmann, O., Kozyrev, A., Krezoski, J.,
 961 Krysak, D., Kuzmin, R., Lacour, J.L., Lafaille, V., Langevin, Y., Lanza, N., Lasue, J., Le
 962 Mouelic, S., Lee, E.M., Lee, Q.-M., Lees, D., Lefavor, M., Lemmon, M., Malvitte, A.L.,
 963 Leshin, L., Leveille, R., Lewin-Carpintier, E., Lewis, K., Li, S., Lipkaman, L., Little, C.,
 964 Litvak, M., Lorigny, E., Lugmair, G., Lundberg, A., Lyness, E., Madsen, M., Mahaffy,
 965 P., Maki, J., Malakhov, A., Malespin, C., Malin, M., Mangold, N., Manhes, G., Manning,
 966 H., Marchand, G., Marin Jimenez, M., Martin Garcia, C., Martin, D., Martin, M.,
 967 Martinez-Frias, J., Martin-Soler, J., Martin-Torres, F.J., Mauchien, P., McAdam, A.,
 968 McCartney, E., McConnochie, T., McCullough, E., McEwan, I., McKay, C., McNair, S.,
 969 Melikechi, N., Meslin, P.-Y., Meyer, M., Mezzacappa, A., Miller, H., Miller, K., Minitti,
 970 M., Mischna, M., Mitrofanov, I., Moersch, J., Mokrousov, M., Molina Jurado, A.,
 971 Moores, J., Mora-Sotomayor, L., Mueller-Mellin, R., Muller, J.-P., Munoz Caro, G.,
 972 Nachon, M., Navarro Lopez, S., Navarro-Gonzalez, R., Nealson, K., Nefian, A., Nelson,
 973 T., Newcombe, M., Newman, C., Nikiforov, S., Niles, P., Nixon, B., Noe Dobrea, E.,
 974 Nolan, T., Oehler, D., Ollila, A., Olson, T., Owen, T., de Pablo Hernandez, M.A., Paillet,
 975 A., Pallier, E., Palucis, M., Parker, T., Parot, Y., Patel, K., Paton, M., Paulsen, G.,
 976 Pavlov, A., Pavri, B., Peinado-Gonzalez, V., Pepin, R., Peret, L., Perez, R., Perrett, G.,
 977 Peterson, J., Pilorget, C., Pinet, P., Pla-Garcia, J., Plante, I., Poitrasson, F., Polkko, J.,
 978 Popa, R., Posiolova, L., Posner, A., Pradler, I., Prats, B., Prokhorov, V., Purdy, S.W.,
 979 Raaen, E., Radziemski, L., Rafkin, S., Ramos, M., Raulin, F., Ravine, M., Reitz, G.,
 980 Renno, N., Richardson, M., Robert, F., Robertson, K., Rodriguez Manfredi, J.A.,
 981 Romeral-Planello, J.J., Rowland, S., Rubin, D., Saccoccio, M., Salamon, A., Sandoval, J.,
 982 Sanin, A., Sans Fuentes, S.A., Saper, L., Sautter, V., Savijarvi, H., Schieber, J., Schmidt,
 983 M., Schmidt, W., Scholes, D.D., Schoppers, M., Schroder, S., Schwenzer, S., Sebastian
 984 Martinez, E., Sengstacken, A., Shterts, R., Siebach, K., Siili, T., Simmonds, J., Sirven, J.-
 985 B., Slavney, S., Sletten, R., Smith, M., Sobron Sanchez, P., Spray, J., Squyres, S.,
 986 Stalport, F., Steele, A., Stein, T., Stern, J., Stewart, N., Stipp, S.L.S., Stoiber, K.,
 987 Sucharski, B., Sullivan, R., Summons, R., Sun, V., Supulver, K., Sutter, B., Szopa, C.,

- 988 Tan, F., Tate, C., Teinturier, S., ten Kate, I., Thomas, P., Thompson, L., Tokar, R.,
989 Toplis, M., Torres Redondo, J., Trainer, M., Tretyakov, V., Urqui-O'Callaghan, R., Van
990 Beek, J., Van Beek, T., VanBommel, S., Varenikov, A., Vasavada, A., Vasconcelos, P.,
991 Vicenzi, E., Vostrukhin, A., Voytek, M., Wadhwa, M., Ward, J., Webster, C., Weigle, E.,
992 Wellington, D., Westall, F., Wiens, R.C., Wilhelm, M.B., Williams, A., Williams, R.,
993 Williams, R.B.M., Wilson, M., Wimmer-Schweingruber, R., Wolff, M., Wong, M.,
994 Wray, J., Wu, M., Yana, C., Yingst, A., Zeitlin, C., Zimdar, R., Zorzano Mier, M.-P.,
995 2014. Mineralogy of a Mudstone at Yellowknife Bay, Gale Crater, Mars. *Science* 343,
996 1243480–1243480. <https://doi.org/10.1126/science.1243480>
- 997 Velbel, M.A., 1999. Bond strength and the relative weathering rates of simple orthosilicates. *Am.*
998 *J. Sci.* 299, 679–696. <https://doi.org/10.2475/ajs.299.7-9.679>
- 999 Volmer, M., Weber, A.Z., 1926. Nucleus Formation in Supersaturated Systems. *Z. Für Phys.*
1000 *Chem.* 119, 277–301.
- 1001 Wade, J., Dyck, B., Palin, R.M., Moore, J.D.P., Smye, A.J., 2017. The divergent fates of
1002 primitive hydrospheric water on Earth and Mars. *Nature* 552, 391–394.
1003 <https://doi.org/10.1038/nature25031>
- 1004 Whipkey, C.E., Capo, R.C., Chadwick, O.A., Stewart, B.W., 2000. The importance of sea spray
1005 to the cation budget of a coastal Hawaiian soil: a strontium isotope approach. *Chem.*
1006 *Geol.* 168, 37–48. [https://doi.org/10.1016/S0009-2541\(00\)00187-X](https://doi.org/10.1016/S0009-2541(00)00187-X)
- 1007 Whipkey, C.E., Capo, R.C., Hsieh, J.C.C., Chadwick, O.A., 2002. Development of Magnesian
1008 Carbonates in Quaternary Soils on the Island of Hawaii. *J. Sediment. Res.* 72, 158–165.
1009 <https://doi.org/10.1306/050801720158>
- 1010 Wordsworth, R., Kalugina, Y., Lokshtanov, S., Vigasin, A., Ehlmann, B., Head, J., Sanders, C.,
1011 Wang, H., 2017. Transient reducing greenhouse warming on early Mars. *Geophys. Res.*
1012 *Lett.* 44, 2016GL071766. <https://doi.org/10.1002/2016GL071766>
- 1013 Wray, J.J., Murchie, S.L., Bishop, J.L., Ehlmann, B.L., Milliken, R.E., Wilhelm, M.B., Seelos,
1014 K.D., Chojnacki, M., 2016. Orbital evidence for more widespread carbonate-bearing
1015 rocks on Mars. *J. Geophys. Res. Planets* 121, 652–677.
1016 <https://doi.org/10.1002/2015JE004972>
- 1017 Zeebe, R., Wolf-Gladrow, D., 2001. CO₂ in Seawater: Equilibrium, Kinetics, Isotopes. Gulf
1018 Professional Publishing.
- 1019

Experiment group name	Initial pH	Maximum duration	DIC concentrations	Initial $p\text{CO}_2$ at initial pH of 2 or 4	Water-rock ratio(s)	Fayalite-forsterite ratio(s)
Low water-rock	2 and 4	60 days	33.51 mmol/kg	1.0 bar	1:1, 1:10	Fa, 1:1 Fa/Fo
Fayalite-bearing	2 and 4	85 days	3.356, 16.79, and 33.51 mmol/kg	0.1, 0.5, 1.0 bar	1:500	Fa
Fayalite-and forsterite-bearing	2 and 4	85 days	3.356, 16.79, and 33.51 mmol/kg	0.1, 0.5, 1.0 bar	1:500	1:1 Fa/Fo, 1:9 Fa/Fo
Non- CO_2	2 and 4	8 days	Non	Non	1:200, 1:500	Fa

Table 1: Table detailing the categories of the 86 experiments conducted in this research.

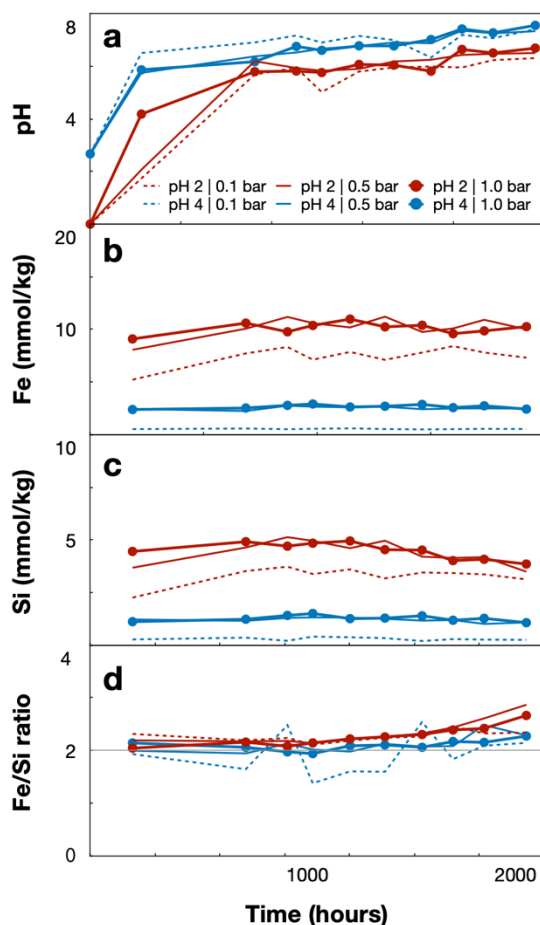


Figure 1: The pH, dissolved Fe and Si, and Fe/Si ratio over time through a typical fayalite-bearing experiment. Note the differing axes. (a) pH for experiments begun at pH 2 or 4, corresponding to equilibration with 0.1 to 1.0 bars of dissolved CO₂ at these initial pHs; (b) Fe concentration over time; (c) Si concentration over time; and (d) the ratio of Fe/Si over time, the stoichiometric ratio in pure fayalite marked as a grey line. Uncertainty for Fe and Si measurements is at 1.2 %; the uncertainty bars for this fall within the thickness of the lines. It is worth noting that $p\text{CO}_2$ depends on pH under a closed system and so will have fluctuated over the course of the experiments. Lines between datapoints are included for ease of following each dataset, and should not be construed as representing exact reaction pathway between datapoints.

[Single column image]

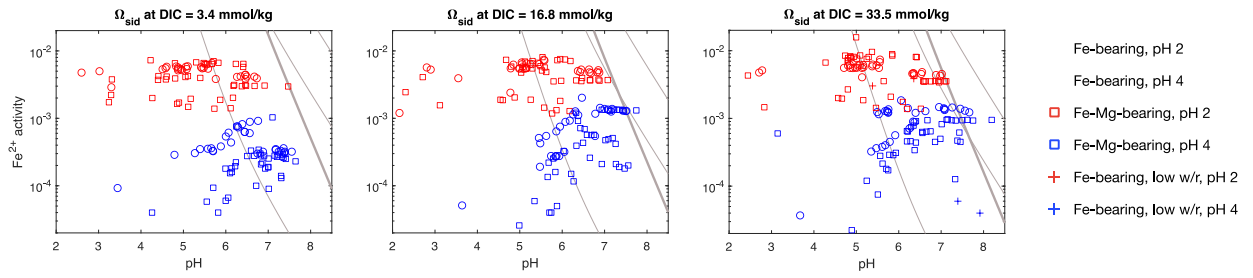


Figure 2: Fe^{2+} activity and pH from solution samples extracted at 10 intervals across 68 experiments, in separate graphs for Ω_{siderite} at DICs of 3.4, 16.8, and 33.5 mmol/kg. Datapoints in red correspond to experiments begun at pH 2; blue for pH 4. Circular datapoints correspond to fayalite-bearing experiments, while squares denote those bearing fayalite and forsterite, and plus-symbols for low water:rock ratio (1:10). pH and Fe^{2+} activity generally increased over the course of an experiment, thus datapoints towards the upper-right generally correspond to increasing reaction times. From left to right, the thin grey lines denote contours of Ω_{siderite} : 1, 400, and 5000. The heavy grey line is the AFC saturation line of Jiang and Tosca (2019).

[Double column image]

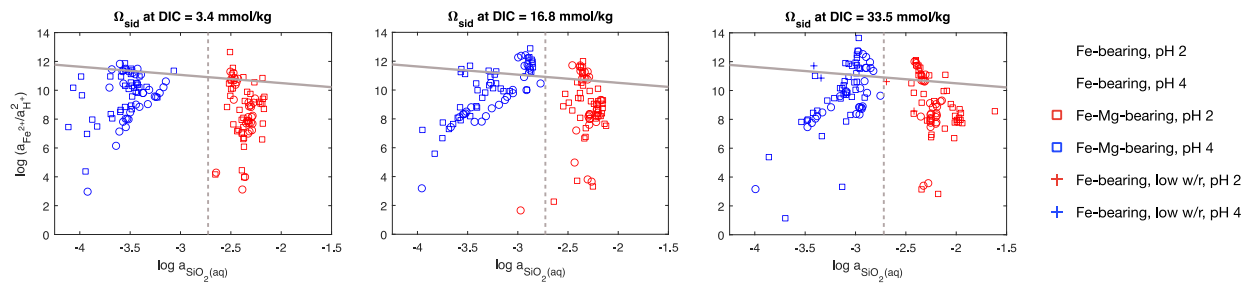


Figure 3: Solubility diagrams for the Fe(II)-silicate system involving the three principal factors controlling greenalite stability. All data are from solution samples extracted at 10 intervals across 68 experiments. Datapoints in red correspond to experiments begun at pH 2; blue for pH 4. Circular datapoints correspond to fayalite-bearing experiments, while squares denote those bearing fayalite and forsterite, and plus-symbols for low water:rock ratio (1:10). Datapoints towards the upper-right generally correspond to increasing reaction times. The heavy grey corresponds to the greenalite saturation (Tosca et al., 2016). The dashed grey line corresponds to amorphous silica saturation (Siever 1992).

[Double column image]

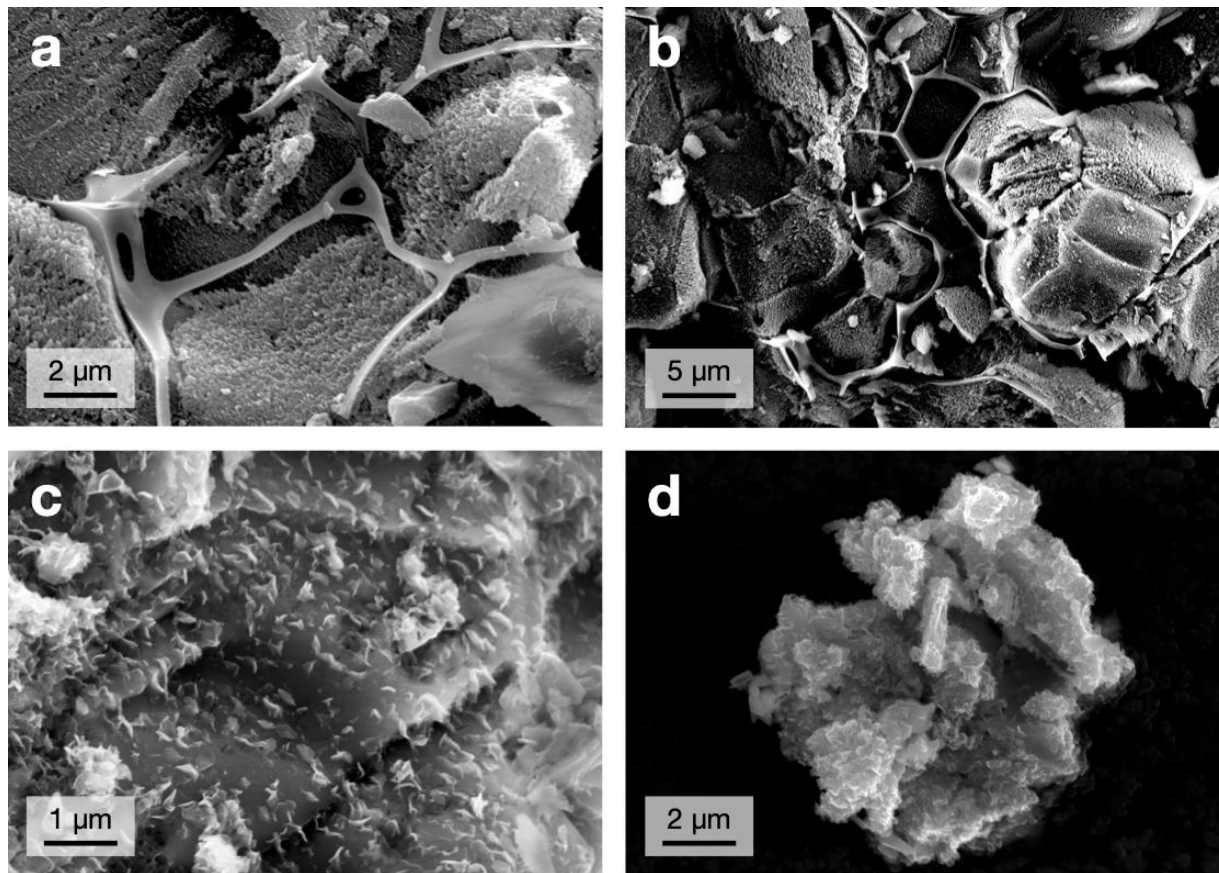


Figure 4: (a) Long, thin, fibrous structures found only upon or between (b) fayalite grains, apparently growing in interstitial spaces and breaking loose when disturbed, as in (a). (c) Aligned, nanometre-scaled precipitates found only upon fayalite grains, or (d) either as individual nuclei apparently formed of the precipitates' coalescence and growth upon each other, or growth upon a separate aggregate.

[Double column image]

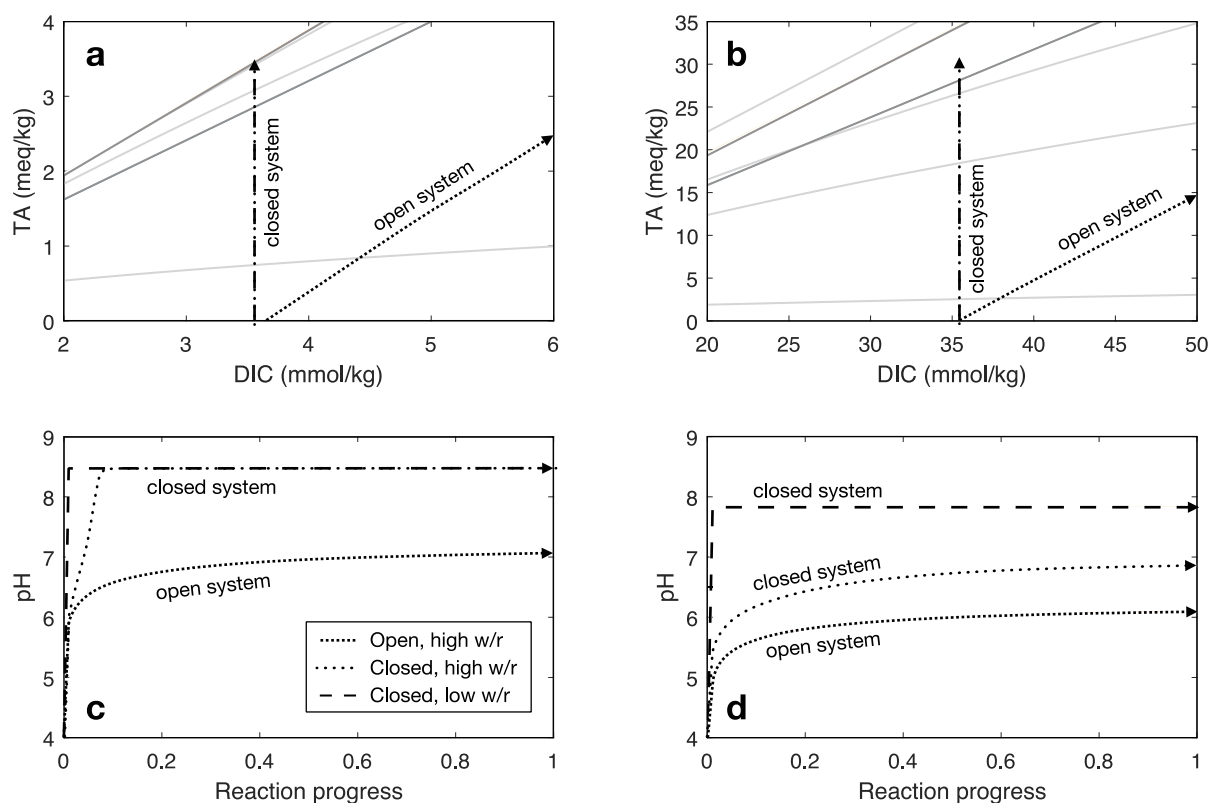


Figure 5: Results from three reaction path models of water-rock interaction at 25 °C: open-system with respect to CO₂ at high water:rock ratio (tightly-dotted lines), closed-system with respect to CO₂ at high water:rock ratio (circular-dotted lines), and closed-system with respect to CO₂ at low water:rock ratio (dashed lines). Left column: models run with 0.1 bar CO₂; right column: models run with 1.0 bar CO₂. (a) and (b): siderite and AFC saturation state as a function of DIC and total alkalinity (TA). From bottom-up, pale-grey lines represent Ω_{siderite} of 1, 100, 400, and 100,000; from bottom-up, dark-grey lines represent an Ω_{AFC} saturation at pH 7 (lower) or 8 (higher). (c) and (d): pH variation over the course of the experiment (which corresponds closely to total alkalinity in this system). In order to illustrate the influence of water-rock interaction on the Fe(II)-carbonate system in DIC-TA space, these models were run under fixed Fe²⁺ concentration of 10 mmol/kg with forsterite as the sole reactant.

[Double column image]

Figure 1

[Click here to download Figure \(high-resolution\): Figure 1.pdf](#)

Figure 2
[Click here to download Figure \(high-resolution\): Figure 2.pdf](#)

Figure 3
[Click here to download Figure \(high-resolution\): Figure 3.pdf](#)

Figure 4

[Click here to download Figure \(high-resolution\): Figure 4.pdf](#)

Figure 5

[Click here to download Figure \(high-resolution\): Figure 5.pdf](#)

Supplementary material for online publication only

[Click here to download Supplementary material for online publication only: Supplementary figures.docx](#)

Supplementary material for online publication only

[Click here to download Supplementary material for online publication only: Supplementary - all data.xlsx](#)

Declaration of interests

☒ The authors declare that they have no known competing financial interests or personal relationships that could have appeared to influence the work reported in this paper.

☐ The authors declare the following financial interests/personal relationships which may be considered as potential competing interests:

Credits

Lucy Kissick: Data curation, formal analysis, investigation, methodology, project administration, software, visualisation, writing: original draft, writing: review and editing.

Tamsin Mather: Supervision, validation, writing: review and editing.

Nicholas Tosca: Conceptualisation, funding acquisition, methodology, project administration, resources, supervision, validation, visualisation, writing: review and editing.